On the thermal structure of the proto-Super Star Cluster 13 in NGC 253

F. Rico-Villas[1]★, E. González-Alfonso[2], J. Martín-Pintado[1], V. M. Rivilla[1], and S. Martín[4,5]
[1]Centro de Astrobiología (CSIC-INTA), Ctra de Ajalvir, km 4, Torrejón de Ardoz, 28850, Madrid, Spain
[2]Universidad de Alcalá, Departamento de Física y Matemáticas, Campus Universitario, Alcalá de Henares, 28871, Madrid, Spain
[3]European Southern Observatory, Alonso de Córdova, 3107, Vitacura, Santiago 763-0355, Chile
[4]Joint ALMA Observatory, Alonso de Córdova, 3107, Vitacura, Santiago 763-0355, Chile

Accepted 2022 July 18. Received YYY; in original form ZZZ

ABSTRACT

Using high angular resolution ALMA observations (0.02″ ≈ 0.34 pc), we study the thermal structure and kinematics of the proto super star cluster 13 in the central region of NGC 253 through their continuum and vibrationally excited HC_3N emission from $J = 24 - 23$ and $J = 26 - 25$ lines arising from vibrational states up to $v_4 = 1$. We have carried 2D-LTE and non-local radiative transfer modelling of the radial profile of the HC_3N and continuum emission in concentric rings of 0.1 pc width. From the 2D-LTE analysis, we found a Super Hot Core (SHC) of 1.5 pc with very high vibrational temperatures (> 500 K), and a jump in the radial velocity (21 km s^{-1}) in the SE-NW direction. From the non-local models, we derive the HC_3N column density, H_2 density and dust temperature ($T_{\rm dust}$) profiles. Our results show that the thermal structure of the SHC is dominated by the greenhouse effect due to the high dust opacity in the IR, leading to an overestimation of the LTE $T_{\rm dust}$ and its derived luminosity. The kinematics and $T_{\rm dust}$ profile of the SHC suggest that star formation was likely triggered by a cloud-cloud collision. We compare proto-SSC 13 to other deeply embedded star-forming regions, and discuss the origin of the $L_{\rm IR}/M_{\rm H_2}$ excess above $\sim 100\,L_\odot\,M_\odot^{-1}$ observed in (U)LIRGs.

Key words: galaxies: individual: NGC 253 – galaxies: ISM – galaxies: nuclei – galaxies: star clusters: general – galaxies: star formation

1 INTRODUCTION

Using high angular resolution ALMA observations (0.02″ ≈ 0.34 pc), we study the thermal structure and kinematics of the proto super star cluster 13 in the central region of NGC 253 through their continuum and vibrationally excited HC_3N emission from $J = 24-23$ and $J = 26 - 25$ lines arising from vibrational states up to $v_4 = 1$. We have carried 2D-LTE and non-local radiative transfer modelling of the radial profile of the HC_3N and continuum emissions. From the 2D-LTE analysis, we found a Super Hot Core (SHC) with high vibrational temperatures (> 500 K), and a jump in the radial velocity (21 km s^{-1}) in the SE-NW direction. From the non-local models, we derive the HC_3N column density, H_2 density and dust temperature ($T_{\rm dust}$) profiles. The thermal structure of the SHC is dominated by the greenhouse effect leading to an overestimation of the LTE $T_{\rm dust}$ and the corresponding luminosities. Star formation seems to be centrally-peaked, supporting the competitive accretion scenario. The formation of the super star cluster was most likely triggered by a cloud-cloud collision as suggested by the kinematics of the SHC. Finally, we compare proto-SSC 13 to other deeply embedded star-forming regions, and discuss the origin of the $L_{\rm IR}/M_{\rm H_2}$ excess above $\sim 100\,L_\odot\,M_\odot^{-1}$ observed in (U)LIRGs.

Even though a large number of SSCs have been observed in different starbursting galaxies (e.g. Melnick et al. 1985; Whitmore et al. 1993; O'Connell et al. 1994; Meurer et al. 1995; Whitmore & Schweizer 1995; Ho & Filippenko 1996b,a; Watson et al. 1996; Whitmore et al. 1999; Gelatt et al. 2001; Tremonti et al. 2001; Vanzi 2003; Turner & Beck 2004; McCrady et al. 2005; Melo et al. 2005; Mengel et al. 2008), most of these studies have been carried out in the UV, optical or near-IR wavelengths (see Portegies Zwart et al. 2010, for a review), detecting relatively evolved SSCs. This is because SSCs remain entirely enshrouded by the large column densities of their natal giant molecular cloud during their formation and earliest phases of evolution, preventing the direct observations of these stages at the aforementioned wavelengths. Therefore, little is known about SSCs during their early evolutionary phases apart from the fact that they need to form most of the stars in a very short timescale before the feedback from massive stars starts to disrupt and disperse the natal cloud (supernovae from the most massive stars take place after $\sim 10^5$ yr of stellar evolution; Bressert et al. 2012; Krumholz et al. 2014), requiring relatively high star formation rates (SFRs) (Beck 2015).

Thanks to ALMA and its high angular resolution and sensitivity, we can now observe high energy molecular lines in the (sub)millimeter range, sampling the hot molecular environments within the obscuring dust regions. This allow us to study the embedded phase of proto-SSCs during their super hot core phase (SHC), a scaled-up version of galactic molecular hot cores (see Rico-Villas et al. 2020). The rotational transitions from vibrationally excited states of HC_3N and HCN, usually excited by mid-IR (e.g. González-Alfonso & Sakamoto 2019), are excellent tracers of the SHC phase. Since HC_3N has a much lower rotational constant ($B_\nu \sim 4.5$ GHz)

★ E-mail: frico@cab.inta-csic.es

than HCN does ($B_\nu \sim 44.4$ GHz) and allows up to seven normal vibrational modes (four stretching modes: ν_1, ν_2, ν_3, ν_4; and three bending modes: ν_5, ν_6 ν_7), it has more rotational transitions in a given wavelength range (1 every ~ 9 GHz), covering a wider energy range. With such many rotational lines from different vibrationally excited states, we are able to study the thermal structure and the kinematics of proto-SSCs with unprecedented detail. This provides the only way to estimate the stellar content in the earliest evolutionary phases of SSCs (proto-SSCs) through the determination of the luminosity of the SHC phase. However, as discussed by Rico-Villas et al. (2020, 2021), the determination of the luminosity from vibrationally excited HC_3N (hereafter HC_3N*) emission is not straightforward due to the back-warming of radiation (Donnison & Williams 1976; Rowan-Robinson 1982; Ivezic & Elitzur 1997). This greenhouse effect produced by the back-warming (González-Alfonso & Sakamoto 2019) is caused by the high column densities ($\gtrsim 10^{25}$ cm^{-2}) and thus high dust opacities, which increase the inner dust temperatures well above the expected dust temperature in the optically thin case. This effect, by increasing the dust temperature and the mid-IR (wavelength responsible for the vibrational excitation of HC_3N) radiation field in the innermost regions, leads to an overestimation of the luminosity of the SHCs. To fully account for this effect and to derive reliable luminosities, the inner thermal structure needs to be derived from spatially resolved observations of the HC_3N* emission.

Such study was done in Rico-Villas et al. (2020) at a resolution of $0.29'' \times 0.19''$ (4.9 pc $\times$ 3.2 pc) for the 14 forming SSCs previously analyzed by Leroy et al. (2018) in the nuclear region of the galaxy NGC 253. This galaxy, located at 3.5 Mpc[1], is one of the closest galaxies hosting a nuclear starburst (for details see Mills et al. 2021). Through the detection of HC_3N* in the $\nu_7 = 1$, $\nu_7 = 2$ and $\nu_6 = 1$ states, Rico-Villas et al. (2020) estimated the luminosity and age of the SSCs in the nuclear region. The high luminosities and young ages proved that they were forming stars at high rates with high star formation efficiencies (SFEs).

In this work, thanks to new ALMA observations at an order of magnitude higher angular resolution of $0.022'' \times 0.020''$ (0.37 pc $\times$ 0.34 pc), we are able to resolve most of the forming SSCs studied in Rico-Villas et al. (2020) and study in detail the inner thermal structure and kinematics from HC_3N* emission in the proto-SSC 13. We selected to study this source in detail because it has one of the brightest continuum emission, was among the youngest sources in Rico-Villas et al. (2020) and has no clear outflow signatures (Levy et al. 2021). We combine the continuum data (at 219 GHz and 345 GHz) and the HC_3N* line emission with non-local radiative transfer models (which include all the high vibrationally excited states detected), to obtain the temperature and density profiles of a proto-SSC, and confirm the presence of the back-warming effect as expected from the high column densities. We also establish that the IR luminosities derived from the HC_3N* emission are overestimated by about an order of magnitude if the greenhouse effect is ignored.

2 OBSERVATIONS

We observed the nuclear region of NGC 253 using the ALMA 12 m Array at very high angular resolution. We performed Band 6 (211 – 275 GHz coverage) observations in ALMA configuration C43-9 (ALMA project 2018.1.01395.S, PI: Rico-Villas, Fernando), which provides the required high angular resolution to resolve most of the proto-SSCs studied in Rico-Villas et al. (2020). In order to observe the maximum number of HC_3N* lines as possible, we optimized the correlator set up by tuning the Local Oscillator at 227.889 GHz, allowing us to record in the lower and upper side bands the frequencies of the $J = 24 - 23$ ($\sim$ 220 GHz) and $J = 26 - 25$ ($\sim$ 237 GHz) HC_3N* rotational transitions. The four spectral windows, with a bandwidth of 1.875 GHz and a channel resolution of 1.3 km s^{-1}, were tuned to cover the frequencies 218.16 – 220.03 GHz and 220.01 – 221.88 GHz for the lower side band, and 234.32 – 236.19 GHz and 236.17 – 238.04 GHz for the upper side band.

Table 1. Log of ALMA Cycle 6 observations NGC 253.

Date (UT)	N. Ant.	Short. Base. (m)	Long. Base. (m)	Int. Time (minutes)
2019-06-06	43	210	15238	44.30
2019-06-08	42	83	16196	44.43
2019-06-09	43	83	16196	44.52
2019-06-10	47	83	16196	44.48
2019-06-12	41	83	16196	44.62
2019-07-10	41	138	13894	44.38

The observations were carried out in six different execution blocks between 2019 June and 2019 July, with an average exposure time on source per execution block of 44.45 minutes, and a total integration time of 4.45 hr. During the observations, short scans of J0006 – 0623 were used for bandpass and flux calibration; J0038−2459 was used for phase calibration. A summary of the observation details can be found in Table 1. The table shows the shortest baselines for each execution block, which set the maximum recoverable scale (MRS[2]) between $0.35''$ and $0.38''$ (5.9 pc and 6.4 pc). This MRS should be enough to assume that the entire flux all the compact SHCs (with sizes < 2 pc Rico-Villas et al. 2020) is recovered. To obtain further information about the dust emission, we used also Band 7 observations from the ALMA project ID: 2017.1.00433.S (PI: Bolatto, Alberto) at $\sim$ 345 GHz. For further details on this observations see Levy et al. (2021).

2.1 Imaging

The visibilities were calibrated using the `CASA`[3] 5.6.1-8 package (Common Astronomy Software Applications, McMullin et al. 2007) pipeline version 42866. For the imaging we then combined the visibilities of the six execution blocks using the `tclean` task from the same `CASA` 5.6.1-8 version. For image cleaning we applied a Briggs weighting scheme, setting the `robust` parameter to 0.5. For masking we used the option `auto-multithresh` to automatically mask regions during the deconvolution (Kepley et al. 2020). The channel width was set to the original spectral resolution of 1 MHz (i.e. $\sim$ 1.3 km s^{-1}). Considering the resulting angular resolution of $\sim 0.025''$, we set the pixel size to $0.007''$ (0.12 pc) to have at least

[1] We have adopted the most common distance assumed in the literature for NGC 253 of $D = 3.5$ Mpc (Rekola et al. 2005). However, recently Anand et al. (2021) and Karachentsev et al. (2021) measured $D = 3.70 \pm 0.12$.

[2] The maximum recoverable scale is the largest angular scale structure that can be recovered by an interferometer and varies with the smallest available baseline ($D_{\rm min}$) and observed wavelength as $\theta_{\rm MRS} \approx 0.6\lambda/D_{\rm min}$ (Cortes et al. 2022).

[3] https://casa.nrao.edu/

Table 2. ALMA ID 2018.1.01395.S project NGC 253 reduced spectral cubes properties. The table lists the covered rest frequencies, the synthesized beam, position angle, channel width and channel rms for each spectral cube.

Rest Freq. (GHz)	Syn. Beam (arcsec^2)	PA (deg)	Ch. width (km s^{-1})	rms (mJy beam^{-1})
218.16 – 220.03	0.026×0.022	42	1.34	0.38
220.01 – 221.88	0.023×0.022	64	1.33	0.35
234.32 – 236.19	0.022×0.020	53	1.24	0.37
236.17 – 238.04	0.022×0.020	47	1.23	0.39

Table 3. NGC 253 continuum map images parameters.

Project ID	Rest Freq. (GHz)	Syn. Beam (arcsec^2)	PA (deg)	rms (μJy beam^{-1})
2018.1.01395.S	219	0.020×0.019	70	13
2017.1.00433.S	345	0.028×0.034	79	37

9 pixels per beam solid angle (i.e. 1.5 times Nyquist sampling). After the imaging, we applied the primary beam correction. Due to the large number of emission and absorption lines expected towards the proto-SSCs, the spectral cubes were imaged from the visibilities without applying a *uv*-plane continuum subtraction. The resulting synthesized beams, channel resolution, covered frequencies and rms for each spectral cube are listed in Table 2. For the spectral cubes, the continuum was subtracted by fitting order 0 baselines. A continuum map (Figure 1), was generated from apparently line-free channels in the *uv*-plane with a synthesized beam of $0.020'' \times 0.019''$ (0.34 pc $\times$ 0.32 pc) and a rms noise of 13 μJy beam^{-1}. However, due to the significant spectral feature contribution mentioned above, the continuum emission in these regions has to be treated with caution.

For the ~ 345 GHz data reduction and calibration of the visibilities we used the `CASA` 5.1.1-5 pipeline version 40896. For the imaging of the *uv*-plane continuum, we selected line emission free channels and used the `tclean` task with the `robust` parameter set to 0.5 and left the default pixel from the pipeline (i.e. $0.005'' = 0.085$ pc). The resulting continuum map at 345 GHz has a resolution of $0.028'' \times 0.034''$ (0.47 pc $\times$ 0.58 pc) and a rms noise of 37 μJy beam^{-1}. A summary of the image details of the continuum maps used in this work is shown in Table 3.

3 THE SPATIAL STRUCTURE OF SSCS

The very high resolution ALMA data (~ 0.40 pc $\times$ 0.35 pc) at ~ 220 – 235 GHz allows us to study in detail the structure and kinematics of the proto-SSCs analysed in Leroy et al. (2018) and Rico-Villas et al. (2020). The study carried out in Rico-Villas et al. (2020) was done at a resolution of $0.29'' \times 0.19''$ (4.9 pc $\times$ 3.2 pc) at ~ 219 GHz. At similar frequencies (218 – 238 GHz), this new data set provides a resolution up to one order of magnitude higher ($0.026'' \times 0.022'' = 0.44$ pc $\times$ 0.38 pc, see Table 2) than our previous analysis. Some of the 14 proto-SSCs studied in Rico-Villas et al. (2020) show clear inner structure with several components (SSCs 14, 13, 12, 11, 10, 8, 5, 4, 3, 1; see Figure 1). This can be seen in the continuum map at 219 GHz in Figure 1, encompassing all the proto-SSCs. The structure of the fragmented proto-SSCs is better illustrated in Figure 2, which shows a zoom-in of the different proto-SSCs. In those cases where the marginally resolved proto-SSCs seen in Rico-Villas et al. (2020) fragment at higher resolution, we label with letters the different components, leaving the label "a" for the region coincident with the position given by Leroy et al. (2018). The coordinates for these regions, based on their peak emission location at 219 GHz, are listed in Table 4. In Figure 1 and Table 4, we also show three positions with 219 GHz continuum emission but a weak counterpart 345 GHz continuum emission labelled SN 1, SN 2 and SN 3. The lower 345 GHz continuum emission indicates a negative spectral index, not associated to dust clumps but rather synchrotron dominated supernovae remnants (SNRs), which seem to be associated to the SNRs in Ulvestad & Antonucci (1997).

Table 4. Coordinates of the peak positions at 219 GHz.

Position	RA (J2000) 00^h47^m	Dec (J2000) $-25°17'$
1a	$32^s.8001$	$21''.220$
1b	$32^s.7939$	$21''.241$
1c	$32^s.8001$	$21''.178$
2	$32^s.8186$	$21''.227$
3a	$32^s.8383$	$21''.101$
3b	$32^s.8377$	$21''.010$
3c	$32^s.8439$	$21''.262$
SN1	$32^s.8770$	$21''.360$
4a	$32^s.9441$	$20''.191$
4b	$32^s.9306$	$20''.310$
4c	$32^s.9327$	$20''.247$
4d	$32^s.9394$	$20''.226$
4e	$32^s.9229$	$20''.338$
5a	$32^s.9859$	$19''.708$
5b	$32^s.9787$	$19''.729$
5c	$32^s.9931$	$19''.624$
5d	$32^s.9977$	$19''.715$
6	$33^s.0112$	$19''.442$
SN2	$33^s.0493$	$18''.833$
7	$33^s.0220$	$19''.078$
8a	$33^s.1144$	$17''.650$
8b	$33^s.1108$	$17''.678$
8c	$33^s.0844$	$17''.692$
9	$33^s.1144$	$18''.182$
10a	$33^s.1531$	$17''.104$
10b	$33^s.1634$	$17''.006$
10c	$33^s.1614$	$17''.146$
10d	$33^s.1696$	$16''.887$
11a	$33^s.1639$	$17''.356$
11b	$33^s.1696$	$17''.475$
12a	$33^s.1753$	$17''.272$
12b	$33^s.1810$	$17''.146$
SN3	$33^s.1934$	$16''.943$
13a	$33^s.1970$	$16''.733$
13b	$33^s.2068$	$16''.691$
13c	$33^s.2145$	$16''.684$
14	$33^s.2955$	$15''.543$

4 PROTO-SSC 13: A CASE STUDY

Our high spatial resolution data clearly shows a large fragmentation on the formation of massive star clusters and SSCs. To better understand the formation of SSCs and their evolution, we need to study the SSCs in their SHC phase (i.e. proto-SSC) in great detail to determine the properties of the different components detected in our maps.

In this work we carry out a detailed study of proto-SSC 13a (i.e.

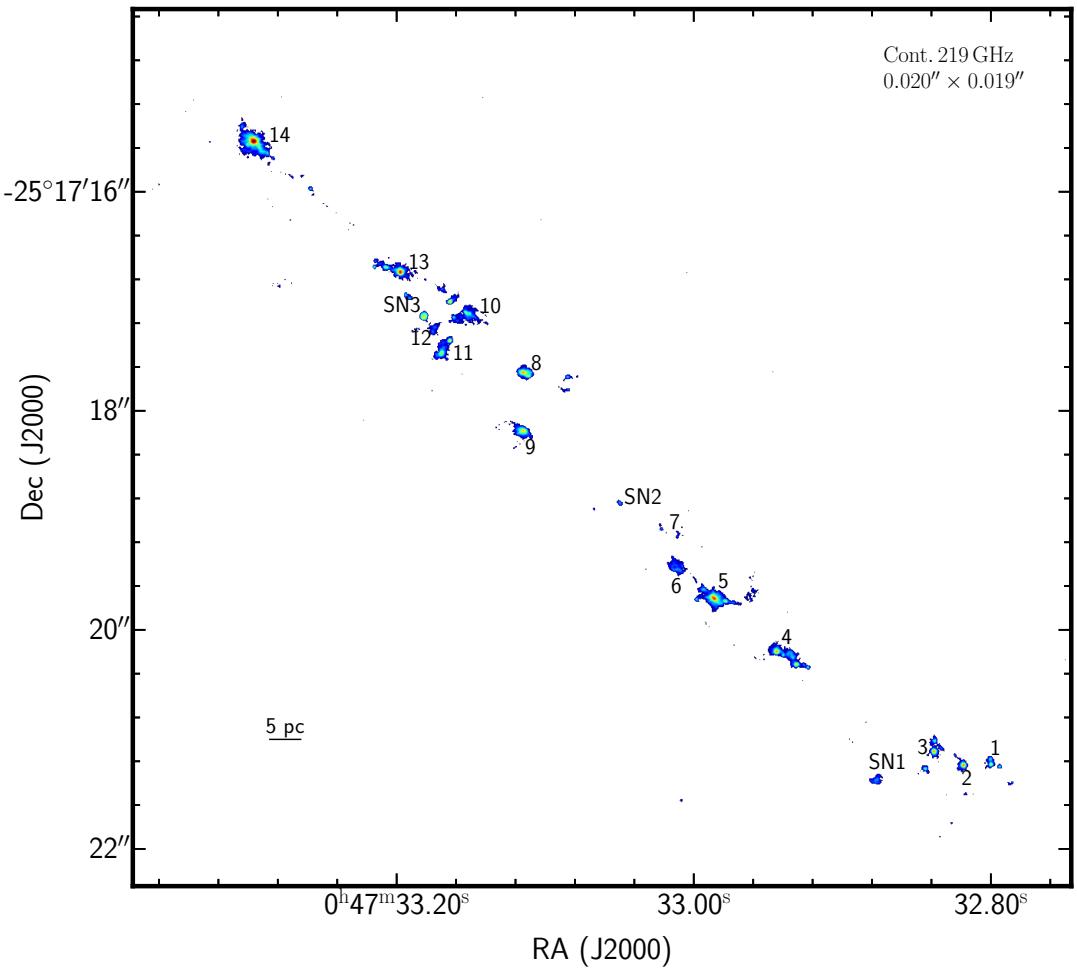

Figure 1. Continuum map at 219 GHz of the NGC 253 nuclear region with a resolution of 0.020″ × 0.019″ above $3\sigma_{219\mathrm{GHz}}$ ($\sigma_{219\mathrm{GHz}}$ = 13 μJy). Labelled are the proto-SSCs studied in Rico-Villas et al. (2020).

SHC 13). The analysis of the other SHCs in forthcoming works will follow the procedure implemented for proto-SSC 13a. Between the two brightest sources at 219 GHz and 345 GHz continuum emission, proto-SSC 13a was selected instead of proto-SSC 14 because the latter, despite showing brighter continuum emission at both frequencies, presents spatially asymmetric emission and complex spectral absorption features in its central region at the HC_3N^* spectral lines. In fact, Levy et al. (2021) recently observed P-Cygni line profiles in the CS 7 – 6 and $H^{13}CN$ 4 – 3 lines in the central region of SSC 14 (also in SSC 4a and SSC 5a), indicative of outflowing gas suggesting a more evolved state of evolution. Since we are interested in understanding the triggering mechanism for the formation of SSCs in galaxies and since there is no evidence for mass ejection in proto-SSC 13a, it is expected to provide a better representation of the very early stages of SSC formation.

In particular, we will address one of the main uncertainties in the previous analysis, the actual luminosities of the SHCs strongly affected by the back-warming (i.e. the greenhouse effect) and the inner kinematics unresolved by previous lower spatial resolution data. In the following sections we present the first study of internal heating of the SHCs combining a multitransition analysis of the spatially resolved HC_3N^* and dust emissions with the modelling of the back-warming effect for different heating scenarios.

4.1 HC_3N^* emission: 2D LTE analysis of proto-SSC 13

Following Rico-Villas et al. (2020), a LTE analysis of the HC_3N^* emission from proto-SSC 13 was carried out with the Spectral Line Identification and Modelling (`SLIM`) module (Martín et al. 2019) within MADCUBA. `SLIM` is a very convenient tool for high spatial resolution spectral analysis since it allows for line identification of spectral features and its LTE analysis (including optical depth effects) directly onto spectral data. We have developed scripts to deal with the 2D determination of the LTE parameters with the `SLIM` multi line analysis including upper limits in both HC_3N column densities and T_{vib}.

Figure 3 shows the integrated intensity (i.e. moment 0) maps of SSC 13 from the HC_3N J = 24 – 23 and J = 26 – 25 rotational transitions in the v = 0 ground state, the v_7 = 1 and v_6 = 1 vibrationally excited states. Among the different emitting regions that conform the proto-SSC 13 (i.e. 13a, 13b and 13c), the only region that shows HC_3N^* emission is 13a, where we will focus our analysis. From the extent of the continuum emission at 219 GHz and 345 GHz, and the emission of the v = 0 transitions, we estimate the radii of the proto-SSC 13a to be $r \approx 1.5$ pc. In the moment 0 maps, in the region where the 219 GHz continuum emission peaks (the central region of SSC 13a) we observe a hole in the emission of the v = 0 lines, and also some decrease of the flux in the v_7 = 1 lines. However, the moment 0 maps from the v_6 = 1 lines do not show such feature. Since

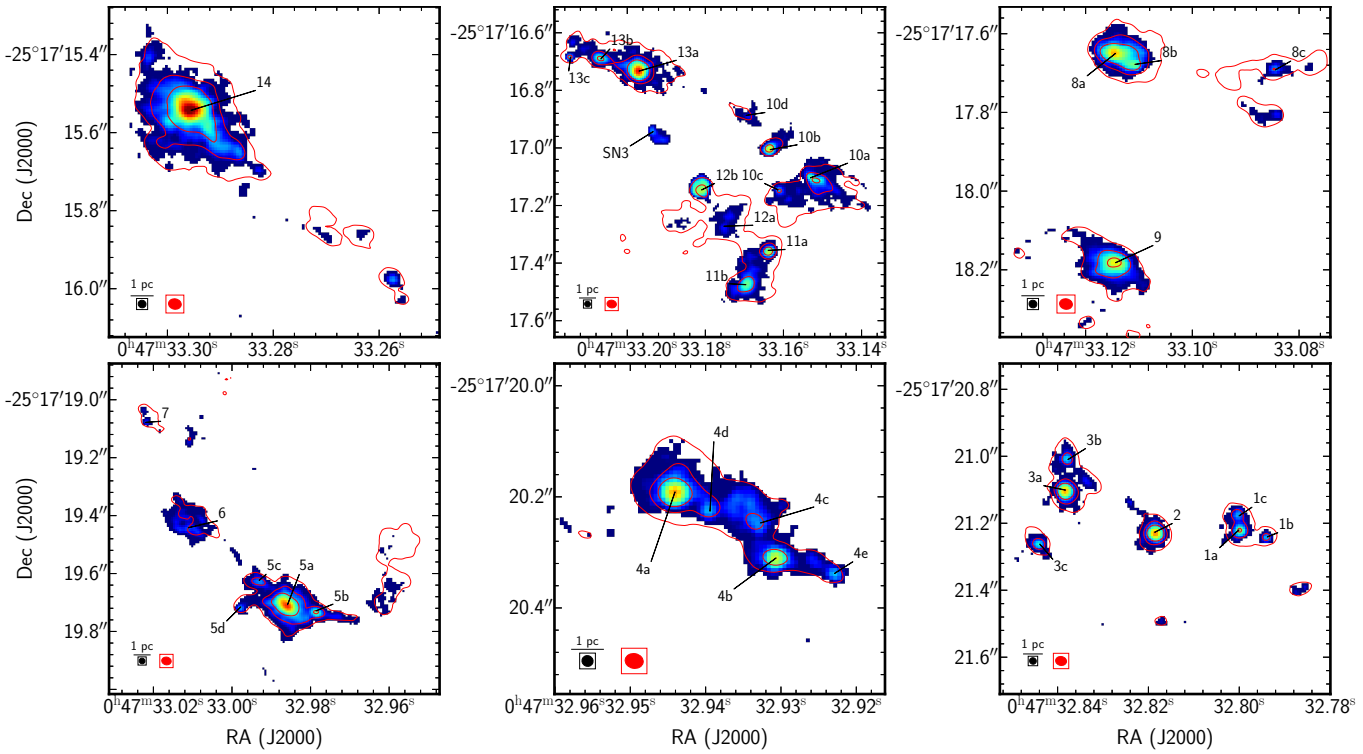

Figure 2. Zoom of the continuum map at 219 GHz above $5\sigma_{219\mathrm{GHz}}$ ($\sigma_{219\mathrm{GHz}} = 13\,\mu\mathrm{Jy\,beam^{-1}}$) for the different regions containing the proto-SSCs studied in Rico-Villas et al. (2020). Overlaid, the continuum emission at 345 GHz is shown in red with contour levels at $5\sigma_{345\mathrm{GHz}}$, $10\sigma_{345\mathrm{GHz}}$, $25\sigma_{345\mathrm{GHz}}$ and $50\sigma_{345\mathrm{GHz}}$ ($\sigma_{345\mathrm{GHz}} = 37\,\mu\mathrm{Jy\,beam^{-1}}$). The different components of each SSC (in which a given SSC is fragmented) are labelled with letters. The 219 GHz beam size ($0.020'' \times 0.019''$; in black) and the 345 GHz beam size ($0.028'' \times 0.0234''$; in red) are plotted, along with a 1 pc scale, on the bottom left-hand corner for reference.

the $v_6 = 1$ transitions arise from higher energies ($E_{\mathrm{up}} > 849$ K) than the $v = 0$ and $v_7 = 1$ lines ($E_{\mathrm{up}} < 475$ K), we consider the decrease in the $v = 0$ and $v_7 = 1$ to be due to absorption of the background continuum and self-absorption in the low-energy transitions instead of a true cavity at the center of proto-SSC 13a. Also, we remind that like in galactic HCs, some uncertainty in estimating the continuum emission is present in the inner regions, where a high spectral density of absorption and emission lines typical in SHCs hamper its estimation.

Besides the rotational transitions arising from the $v = 0$, $v_7 = 1$ and $v_6 = 1$ states, other HC_3N^* $J = 24-23$ and $J = 26-25$ rotational transitions from even higher vibrationally excited states also lie in the analysed spectral range. These vibrational excited states are $v_7 = 2$, $v_5 = 1/v_7 = 3$, $v_6 = v_7 = 1$, $v_7 = 4/v_5 = v_7 = 1$, $v_6 = 2$, $v_4 = v_7 = 1$ and $v_4 = 1, v_7 = 2/v_5 = 2^0$ (see Table B1). However, as shown in Rico-Villas et al. (2020), the proto-SSCs like proto-SSC 13a have an extremely rich chemistry and a very prominent molecular line emission from many other species, making several HC_3N^* transitions to be blended with transitions from other molecules. This makes that some of the weaker high-energy[4] HC_3N^* emission lines to be blended with other species. We have been able to confirm the detection of clean or only slightly-blended HC_3N^* emission in the $v = 0$ vibrational ground state and in the $v_7 = 1$, $v_7 = 2$, $v_6 = 1$, $v_5 = 1/v_7 = 3$, $v_6 = v_7 = 1$ and $v_4 = 1$ vibrationally excited states (see Figure A2). Transitions from the $v_7 = 4/v_5 = v_7 = 1$ vibrational state are strongly blended with other lines. For higher vibrational states ($v_6 = 2$ and $v_4 = v_7 = 1$), the expected line strength (from the CDMS[5] catalogue; Müller et al. 2001, 2005) decreases by more than a 45% with respect to that of the $v_4 = 1$ $J = 26 - 25$ transition (detected only in the most central region), and therefore are not detected. A summary of the HC_3N^* transitions in the observed spectral range, with their quantum numbers, energy of the upper state of the transition, frequencies, Einstein-A_{ul} coefficients, line strengths and if they are detected and contaminated is shown in Table B1.

To improve the signal-to-noise ratio for the LTE modelling, we have smoothed the spectral resolution to half the original value, down to $\sim 2.5\,\mathrm{km\,s^{-1}}$. Figures inside Appendix A show the averaged spectra within rings centered on proto-SSC 13, (see Section 4.2 for the definition of these rings) with all the HC_3N^* transitions and other identified species also indicated for completeness. Those HC_3N^* lines that are blended with a line from another species but with only one transition observed for this species, are not considered for the SLIM LTE modelling since we cannot properly estimate the degree of blending. In case it is partially blended with another species with more than one observed transition, we also model these species and deblend its emission from that of the HC_3N^* emission with SLIM assuming the emission from the other species can be properly fitted under LTE. Also, for the central pixels within a region of ≈ 0.45 pc, we ignored the HC_3N rotational lines from the lowest vibrational

[4] We will refer to low-energy HC_3N^* lines to the rotational transitions arising from the ground state $v = 0$ and the $v_7 = 1$ vibrationally excited state. Similarly, high-energy transitions will be those with $E_{\mathrm{lo}} > 1000$ K, i.e. those from the $v_5 = 1/v_7 = 3$, $v_6 = v_7 = 1$, $v_4 = 1$ and $v_6 = 2$ vibrational states.

[5] http://www.astro.uni-koeln.de/cgi-bin/cdmssearch

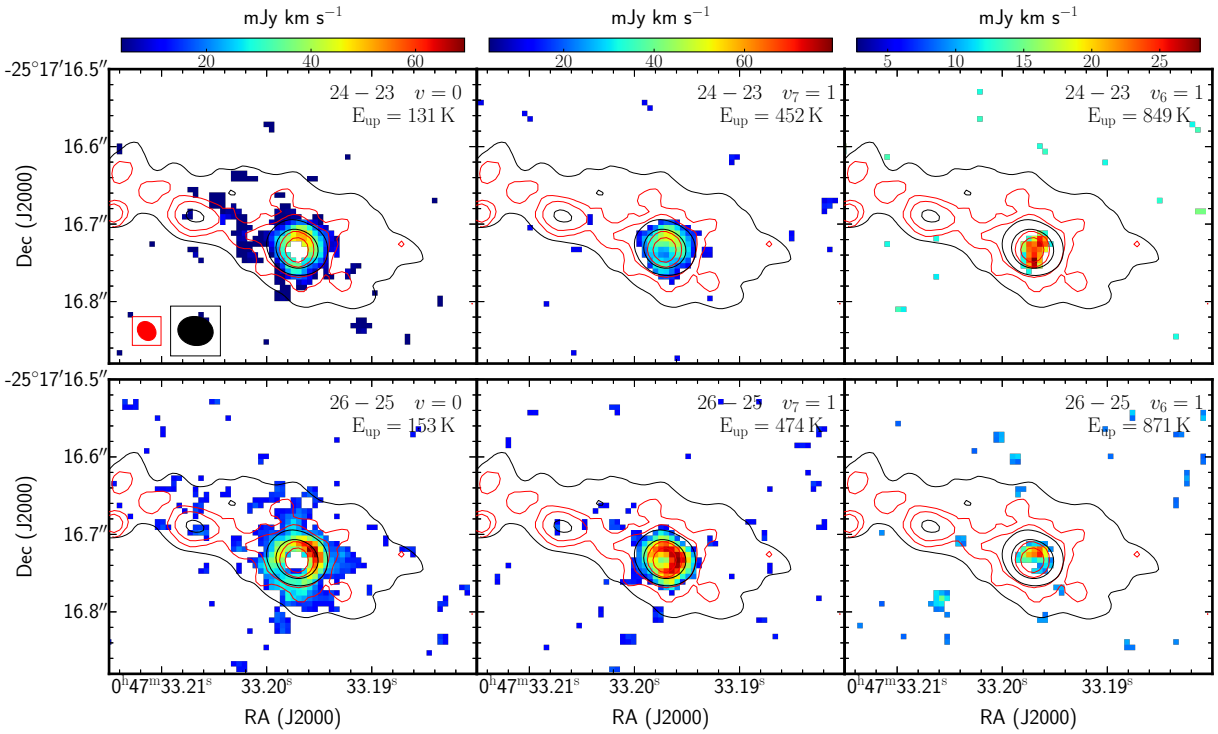

Figure 3. SSC 13 HC_3N* moment 0 maps. The left panels show the $J = 24 - 23$ (top) and the $J = 26 - 25$ (bottom) rotational transitions from the $v = 0$ state. The middle panels show the $J = 24 - 23$ $l_{up} = 1$ (top) and the $J = 26 - 25$ $l_{up} = 1$ (bottom) rotational transitions from the $v_7 = 1$ vibrational state. The right panels show the $J = 24 - 23$ $l_{up} = -1$ (top) and the $J = 26 - 25$ $l_{up} = -1$ (bottom) rotational transitions from the $v_6 = 1$ vibrational state. Overlaid with red and black contours are the 5σ, 10σ, 50σ and 100σ levels from the 219 GHz and 345 GHz continuum emission, respectively. Top left panel shows the beam sizes of the 219 GHz (in red) and the 345 GHz (in black) continuum emission.

states $v = 0$ and $v_7 = 1$ because they are affected by strong absorption of the continuum and self-absorption (see Figure 3). Therefore, for the SLIM LTE modelling of the central region, we only considered transitions from vibrationally excited states with the highest energies, which are expected to be less affected by absorption.

Following the above procedure, we have developed MADCUBA scripts to carry the HC_3N* LTE modelling of the HC_3N* emission with SLIM for all pixels of the proto-SSC 13a emitting region. In order to obtain the vibrational temperature (T_{vib}) and the total HC_3N column density ($N(HC_3N)$), we have modelled the HC_3N* $J = 24-23$ and $J = 26-25$ rotational transitions from all (excluding the $v = 0$ and $v_7 = 1$ transitions in the central pixels, see above) the vibrationally excited states and the ground state simultaneously with a single temperature (i.e. the vibrational temperature T_{vib}). Unfortunately, the small energy difference between the $J = 24 - 23$ and the $26 - 25$ lines and the high T_{vib} did not allow us to estimate the rotational temperature T_{rot}. However, as seen in Rico-Villas et al. (2020, 2021); Costagliola & Aalto (2010), we expect T_{rot} to be lower than T_{vib}. For those pixels where HC_3N from the $v = 0$ is detected but HC_3N* (from the $v_7 = 1$) is not, we estimated an upper limit for T_{vib} (SLIM calculates these upper limits by using the 3σ upper limit to the $v_7 = 1$ column density and the fitted column density of the $v = 0$ transition). The pixels where no HC_3N emission is detected (i.e. no HC_3N from the ground and vibrationally states) were masked with the estimated upper limits to the HC_3N column density with SLIM (based on the rms noise of the integrated line intensity; for details, see Martín et al. 2019) assuming a $T_{vib} \sim 150$ K (close to the median upper limit $T_{vib} \sim 161$ K), and fixing the full width at half maximum (FWHM) to 30 km s^{-1} (close to the values where HC_3N is detected) and the velocity of the local standard of rest (V_{LSR}) to 250 km s^{-1} (the mean V_{LSR} for SSC 13). We note that these $N(HC_3N)$ upper limits are conservative and probably overestimate the column density since they are obtained assuming a high excitation temperature. Figure 4 shows the HC_3N column density, vibrational temperature, V_{LSR} and FWHM map values derived with SLIM.

From Figure 4 we can see that the region with highest HC_3N column densities ($\gtrsim 10^{16}$ cm^{-2}) is the region where we also find the highest temperatures ($T_{vib} \gtrsim 400$ K). There is a decrease in the column density towards the center of proto-SSC 13a coincident with the highest temperatures. This is a spurious effect probably caused by the high opacity towards the center. Also, while the temperature map appears symmetric, the column density map seems to be slightly elongated in the NE-SW direction along the galaxy disk, where we find a bridge of emission joining 13a with 13b, see Fig. 2. Lower left and lower right panels of Figure 4 show the velocity and the FWHM maps derived from HC_3N* SLIM modelling. As derived in Rico-Villas et al. (2020), proto-SSC 13a has a systemic velocity of 250 km s^{-1}. Figure 4 clearly shows a sharp jump in the velocity along the SE-NW direction (i.e. perpendicular to NGC 253 rotation disk, with PA= 55°; Krieger et al. 2019), dividing the region with $T_{vib} \gtrsim 500$ K. Perpendicular to this local velocity change, i.e. the region with velocities ~ 250 km s^{-1} along NGC 253 disk, we can see that the HC_3N* FWHMs are also larger (~ 35 km s^{-1}). The possible nature and implications of the ~ 21 km s^{-1} jump between the minimum (242 km s^{-1}) and maximum (263 km s^{-1}) velocities is discussed in Section 5.4.

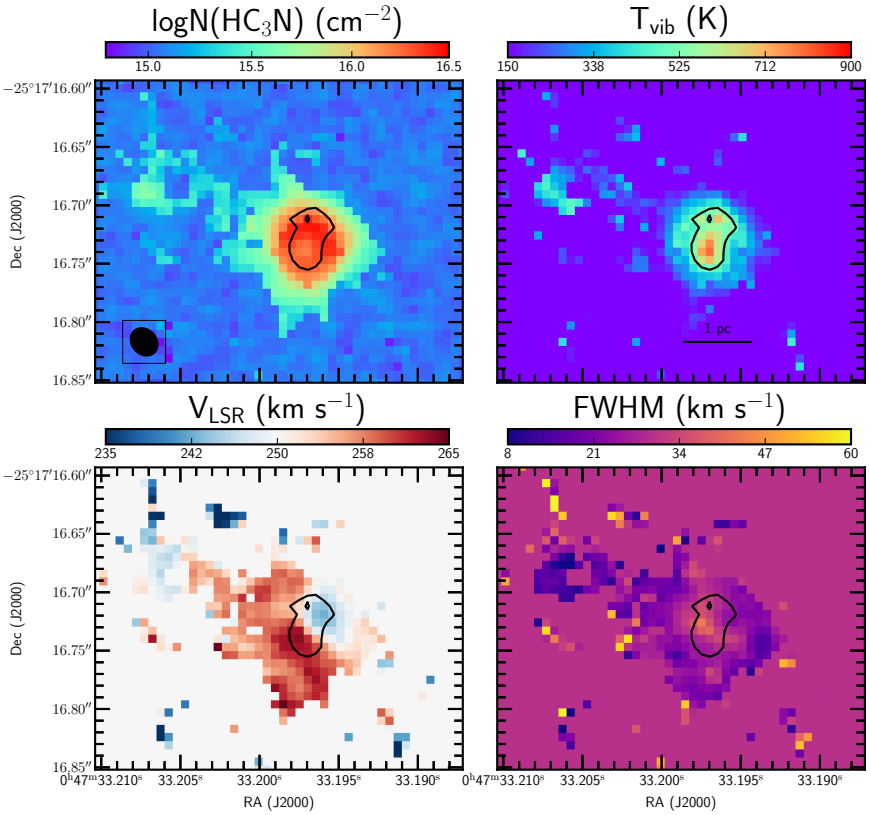

Figure 4. Proto-SSC 13 LTE fitted values with SLIM. Top left panel shows the HC_3N column density, top right panel the vibrational temperature, bottom left the V_{LSR} and bottom right the FWHM. The black contour indicates the region with $T_{vib} > 500$ K. To estimate upper limits to the column density we have fixed T_{vib} to 150 K, the V_{LSR} to 250 km s^{-1} and the FWHM to 30 km s^{-1}, and therefore these values appear as background pixels.

Table 5. Velocity integrated line intensities of ring averaged spectra in proto-SSC 13.

Dist.		$v = 0$	$v_7 = 1$	$v_7 = 1$	$v_7 = 2$	$v_7 = 2$	$v_6 = 1$	$v_6 = 1$	$v_5 = 1/v_7 = 3$	$v_6 = v_7 = 1$	$v_4 = 1$	$v_6 = 2$
	J_{up}-J_{lo}	26–25	24–23	26–25	24–23	26–25	24–23	26–25	26–25	26–25	26–25	24–23
	l_{up}; l_{lo}		1; -1	1; -1	0; 0	0; 0	-1; 1	-1; 1	1,0; -1,0	2,2; -2,2		0; 0
(pc)	ν (GHz)	236.51	219.17	237.43	219.68	237.97	218.68	236.90	236.66	237.81	236.18	219.02
0.05		$\leqslant 9.3$	27.2 ± 3.2	37.8 ± 1.9	28.6 ± 3.5	30.4 ± 2.2	27.9 ± 3.1	30.7 ± 2.2	19.1 ± 2.1	19.1 ± 1.6	12.9 ± 1.7	$\leqslant 9.4$
0.15		21.1 ± 2.3	31.1 ± 2.2	42.2 ± 1.4	28.1 ± 2.5	30.5 ± 1.6	26.7 ± 2.2	29.9 ± 1.6	17.8 ± 1.5	16.0 ± 1.1	10.1 ± 1.2	$\leqslant 6.8$
0.25		41.8 ± 1.5	37.0 ± 1.7	45.1 ± 1.0	24.4 ± 1.7	28.4 ± 1.0	23.6 ± 1.5	25.4 ± 1.1	15.8 ± 1.1	12.9 ± 0.7	5.8 ± 0.7	$\leqslant 4.9$
0.35		52.6 ± 1.3	40.9 ± 1.6	42.0 ± 0.8	20.0 ± 1.4	23.6 ± 0.8	18.7 ± 1.3	17.0 ± 0.9	10.2 ± 0.8	8.8 ± 0.6	3.5 ± 0.6	$\leqslant 4.1$
0.45		50.5 ± 1.3	33.7 ± 1.2	34.0 ± 0.8	17.1 ± 1.2	17.6 ± 0.8	11.9 ± 1.0	10.3 ± 0.9	5.4 ± 0.7	4.4 ± 0.5	1.7 ± 0.4	$\leqslant 2.9$
0.55		41.2 ± 1.1	22.0 ± 1.2	24.4 ± 0.7	10.9 ± 1.3	11.5 ± 0.7	6.0 ± 1.1	4.9 ± 0.8	$\leqslant 1.9$	$\leqslant 1.4$	1.0 ± 0.3	$\leqslant 3.0$
0.65		30.4 ± 1.0	14.4 ± 1.1	14.6 ± 0.6	6.4 ± 1.2	6.6 ± 0.7	$\leqslant 2.9$	3.9 ± 0.7	$\leqslant 1.7$	$\leqslant 1.0$	$\leqslant 0.9$	$\leqslant 2.6$
0.75		21.8 ± 0.8	7.0 ± 1.0	6.6 ± 0.5	$\leqslant 3.3$	3.9 ± 0.5	$\leqslant 2.9$	2.2 ± 0.6	$\leqslant 1.4$	$\leqslant 0.9$	$\leqslant 0.8$	$\leqslant 2.4$
0.85		18.3 ± 0.8	3.9 ± 0.9	2.4 ± 0.5	$\leqslant 3.3$	2.9 ± 0.6	$\leqslant 3.0$	$\leqslant 1.9$	$\leqslant 1.5$	$\leqslant 0.9$	$\leqslant 0.8$	$\leqslant 2.7$
0.95		14.7 ± 0.7	2.7 ± 0.9	1.7 ± 0.5	$\leqslant 3.0$	2.0 ± 0.5	$\leqslant 2.7$	$\leqslant 1.7$	$\leqslant 1.4$	$\leqslant 0.8$	$\leqslant 0.8$	$\leqslant 2.8$
1.05		10.6 ± 0.7	$\leqslant 2.4$	1.9 ± 0.5		$\leqslant 1.6$		$\leqslant 1.3$				
1.15		7.9 ± 0.7	$\leqslant 2.0$	1.6 ± 0.5		$\leqslant 1.6$		$\leqslant 1.3$				
1.25		7.3 ± 0.7	$\leqslant 2.0$	$\leqslant 1.4$		$\leqslant 1.5$		$\leqslant 1.2$				
1.35		7.5 ± 0.6	$\leqslant 1.5$	$\leqslant 1.1$		$\leqslant 1.5$		$\leqslant 1.0$				
1.45		5.8 ± 0.6	$\leqslant 1.5$	$\leqslant 1.1$		$\leqslant 1.2$		$\leqslant 1.0$				

Note. The table lists the distance in pc to each averaged ring (i.e. $(R_{int} + R_{out})/2$) with the line intensities in Jy km s^{-1} beam^{-1}. The table also lists the quantum numbers and the frequency of the transition in GHz.
The $v_5 = 1/v_7 = 3$ and $v_6 = v_7 = 1$ quantum numbers refer to l_{up}, k_{up}; l_{lo}, k_{lo}.
The $v_6 = 2$ 24, 0 – 23, 0 transition is not detected in any ring, but its upper limits are included as a consistency test for the non-local radiative transfer models.

4.2 Radial distribution of proto-SSC 13a: LTE-SLIM analysis

To increase the signal-to-noise ratio of the spectra, specially for the higher energy lines, and thus improve our analysis, we have averaged the spectra within rings of 0.1 pc thickness with radius increasing in 0.1 pc up to 1.5 pc, as the noise decreases with the considered number of pixels for each ring like $1/\sqrt{N_{\rm px}}$. This is appropriate for proto-SSC 13a since it appears to be rather symmetric (e.g. see Figure 4), with the rings centered on the pixel with the brightest continuum emission at 219 GHz (RA(J2000)= $00^{\rm h}47^{\rm m}33^{\rm s}.1970$; Dec(J2000)= $-25°17'16''.733$). Table 5 lists the integrated line intensities of the HC_3N* transitions within the rings.

With SLIM, we have modelled the emission of these higher signal-to-noise ratio averaged ring spectra following the same LTE procedure described above. Figures in the Appendix A (available in the online version) show the HC_3N* LTE modelled emission for the rings. We have observed that at short distances ($r < 0.4$ pc), HC_3N* transitions from the $v = 0$ and $v_7 = 1$ states show strong absorption and therefore, as described above, were not taken into account for the fit. Although for these self-absorbed, contaminated or at noise level line profiles are simulated with SLIM for the derived parameters, they are not taken into account for the fitting. Therefore, some undetected lines from high vibrational states show modelled emission within noise level. Obviously, the SLIM models cannot reproduce all HC_3N* lines simultaneously due to non-local effects that are not included. In addition, since line absorption is more important for low-energy lines than for high-energy lines, SLIM considers their ratio as very high $T_{\rm vib}$. We can thus consider the SLIM $T_{\rm vib}$ (i.e. $T_{\rm dust}$, see Rico-Villas et al. 2020) in the innermost regions as upper limits.

Table 6 lists the distance to each ring, the number of pixels contained in the ring, and the weighted mean values (for the pixels within each ring that are not upper limits) of $T_{\rm vib}$ and $N(HC_3N)$ from the fit to the spectra of individual pixels in the image (for the pixels within each ring that are not upper limits), together with the corresponding values inferred from the averaged ring spectra. These values are plotted as a function of their distance to proto-SSC 13a center in Figure 5. There is a good match between both profiles, but there is a clear improvement in the error of the estimated parameters in the averaged spectra, specially in the lower signal to noise regions.

Figure 5 show that $T_{\rm vib}$ peaks at the central pixel ($T_{\rm vib} \lesssim 751$ K) and decreases with distance to ~ 200 K at 0.85 pc. At longer distances ($\gtrsim 0.9$ pc), most pixels have $T_{\rm vib}$ upper limits (i.e. no HC_3N $v_7 = 1$ line was detected) with $T_{\rm vib} \lesssim 186$ K. For the HC_3N* column density, its maximum value is obtained at ~ 0.25 pc. The lower column density values at smaller distances are probably an artifact produced by the strong absorption towards the central region, which still affects even the strength of the $v_6 = 1$ and $v_7 = 2$ lines. We note that the fitted averaged spectra values start to differ from the pixel mean values at distances $\gtrsim 1.0$ pc as a result of averaging all pixels (with and without HC_3N* column density upper limits in each individual pixel).

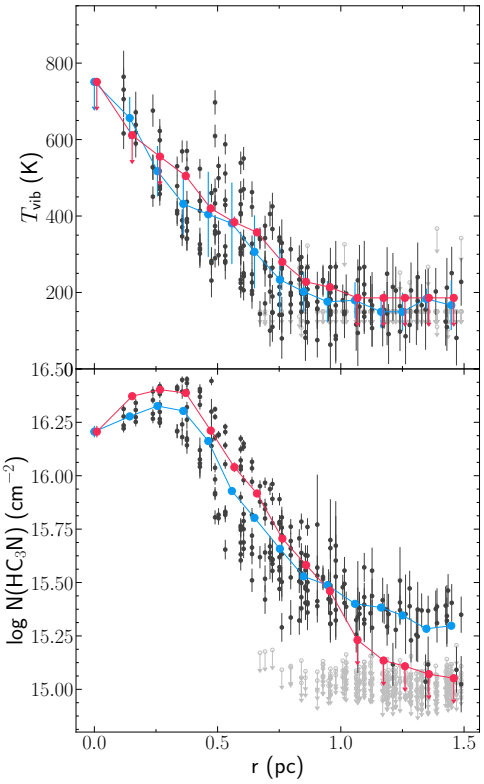

Figure 5. Proto-SSC 13a HC_3N* vibrational temperature ($T_{\rm vib}$) and column density ($\log N(HC_3N)$) profiles derived from the LTE model fitting with SLIM from Table 6. Solid black dots represent the values fitted for each individual pixel, while grey markers with arrows represent upper limits for each individual pixel. Blue markers show the weighted mean of the fitted values for the pixels (not considering the upper limits) within each ring of 0.1 pc thickness. Red markers show the fitted values for the averaged spectra of each ring.

4.3 Radial distribution of proto-SSC 13a: Non-local analysis

As seen in Rico-Villas et al. (2020), LTE can be assumed for the excitation of the HC_3N* emission when there is a strong IR radiation field and a high dust optical depth in the mid-IR. This is because HC_3N molecules will be immersed in a local radiation field described by a blackbody at the dust temperature (i.e. $T_{\rm vib} \sim T_{\rm dust}$) and their ro-vibrational transitions (excited by $\sim 11 - 45$ µm radiation) will be thermalized independently from their Einstein-A_{ul} coefficients and H_2 density. However, the large column densities that in principle validate LTE excitation, make non-local radiative transfer effects very important: the large amounts of gas and dust increase the probabilities for a photon emitted in some region at that local $T_{\rm dust}$ to be absorbed in another region at $T'_{\rm dust}$, even more than once, before reaching the observer. In addition, in the case of density and temperature gradients within the SHCs, the high line opacities will make every line to trace different excitation temperatures. We have then carried non-local radiative transfer models of the HC_3N* emission assuming LTE excitation for all states. We have assumed LTE excitation since, as already mentioned, all HC_3N* lines are expected to be thermalized at $T_{\rm dust}$. Also, the A_{ul} coefficients from many of the ro-vibrational bands are not available, preventing to carry a full non-LTE excitation modelling for all the observed lines.

The radiative transfer models are based on the radiative transfer code developed by González-Alfonso & Cernicharo (1997, 1999) and González-Alfonso & Sakamoto (2019), with the inclusion of the $v_5 = 1/v_7 = 3$, $v_6 = v_7 = 1$, $v_4 = 1$ and $v_6 = 2$ vibrationally excited states up to high J values ($J = 50$) and assuming thermalisation (i.e. local LTE excitation). These models aim at reproducing the spatial profile of the emission from the detected, unblended and uncontaminated HC_3N* transitions listed in Table 5. These transitions cover a wide range of energies, from 142 K to 1579 K. The $v_6 = 2$ $(24, 0 - 23, 0)$ transition is not detected and is included in the models as a control to the HC_3N column density and vibrational temperature. Emission lines are self-consistently fitted together with the radial profiles of

Table 6. Proto-SSC 13a HC_3N* vibrational temperature and column density comparison between the average of fitted pixels and the fit to the average spectrum for each ring.

		Pixels mean		Averaged spectra	
Dist. (pc)	# Pixels	T_{vib} (K)	$\log N(HC_3N)$ (cm^{-2})	T_{vib} (K)	$\log N(HC_3N)$ (cm^{-2})
0.05	1	$\leqslant 751$	16.21 ± 0.02	$\leqslant 751$	16.21 ± 0.03
0.15	8	656 ± 55	16.28 ± 0.04	$\leqslant 611$	16.37 ± 0.02
0.25	12	517 ± 66	16.33 ± 0.06	$\leqslant 555$	16.40 ± 0.02
0.35	16	432 ± 79	16.30 ± 0.11	505 ± 26	16.39 ± 0.02
0.45	20	404 ± 111	16.16 ± 0.18	420 ± 37	16.21 ± 0.02
0.55	24	381 ± 107	15.93 ± 0.20	384 ± 35	16.04 ± 0.03
0.65	28	306 ± 96	15.80 ± 0.19	357 ± 34	15.92 ± 0.02
0.75	36	234 ± 84	15.66 ± 0.15	280 ± 30	15.71 ± 0.02
0.85	32	202 ± 52	15.53 ± 0.12	228 ± 21	15.58 ± 0.02
0.95	44	176 ± 54	15.49 ± 0.13	214 ± 22	15.46 ± 0.02
1.05	56	179 ± 47	15.40 ± 0.09	$\leqslant 186$	$\leqslant 15.23$
1.15	48	149 ± 43	15.38 ± 0.08	$\leqslant 186$	$\leqslant 15.13$
1.25	48	149 ± 50	15.35 ± 0.12	$\leqslant 186$	$\leqslant 15.11$
1.35	64	183 ± 27	15.28 ± 0.12	$\leqslant 186$	$\leqslant 15.07$
1.45	60	167 ± 65	15.30 ± 0.15	$\leqslant 186$	$\leqslant 15.05$

Note. (1) Ring distance. (2) Number of pixels in each ring. (3) Weighted mean of the LTE vibrational temperature fitted for each pixel within the ring. The errors, except for ring 1 with one single pixel, are the errors of the mean. (4) Weighted mean of the LTE column density fitted for each pixel within the ring. The errors, except for the first ring with one single pixel, are the errors of the mean. (5) Fitted LTE vibrational temperature to the ring averaged spectra (i.e. the spectra obtained from averaging all the spectra from the pixels within each ring). (6) Fitted LTE column density to the ring averaged spectra.

the continuum emission at 235 GHz and 345 GHz obtained from the ring spectra (top left panel of Figure 6).

Regarding the thermal structure of the SHC, we have used different density and T_{dust} radial profiles derived following González-Alfonso & Sakamoto (2019), which take into account the greenhouse effect expected for the very large column densities ($N_{H_2} > 10^{24}$) derived in Rico-Villas et al. (2020). The T_{dust} profiles are obtained in a self-consistent way considering the heating and cooling of dust grains in a spherical cloud with a given density profile. Input model parameters are the luminosity surface density $\Sigma_{IR} = L_{IR}/(\pi R^2)$, the H_2 column density $N(H_2)$, the density profile (parameterized with q as $n_{H_2} \propto r^{-q}$) and the absorption coefficient of dust as a function of wavelength $\kappa_{abs}(\lambda)$. The derived temperature profiles also depend on the nature of the heating source (point source and centrally-peaked). For the case of SSCs, we use the centrally peaked starburst profiles from González-Alfonso & Sakamoto (2019), which consider the deposition of energy due to star formation to be distributed across the cloud and proportional to the shell density and mass, in contrast with a single point source heating, expected for the AGN models (González-Alfonso & Sakamoto 2019). The models are then described by the source radius r_{out}, a total L_{IR}, a total gas H_2 column density N_{H_2} and the density profile power-law index q. These parameters define consistently the T_{dust} profile for the type of heating (star formation or AGN) used in our radiative transfer predictions. Hence, the only free-parameters are the HC_3N abundance relative to H_2 (X_{HC_3N}), which we vary for each shell to fit the observed spatial profiles, and X_d which reflects the amount of dust relative to gas (by mass).

We find that the ratio between the 235 GHz and 345 GHz continuum emission increases for $r < 0.85$ pc (once corrected for the different beams), indicating the presence of free-free emission. To account for this free-free emission observed at the center we use the X_d parameter, which is boosted in the central region to mimic such free-free emission. For $r < 0.85$ pc, the extra continuum added accounts for a total of 1.89 mJy at 235 GHz, very similar to the estimated non-dust contribution ($S_{219_{n\text{-}dust}} = 1.99$ mJy) obtained by assuming a spectral index expected for optically thin dust emission of $\alpha_{345-219} \sim 3.5$. In the outer region (i.e. $r \gtrsim 0.85$ pc), X_d is also adjusted to fit the observed 235 GHz emission, which translates into a higher column and mass of gas and dust relative to the power-law density profile. This is because no single value of q can describe the whole spatial profile of the observed continuum emission. Accordingly, we consider the excess of dust added up to 0.85 pc as free-free emission and from 0.85 pc to 1.5 pc as an increase in mass that deviates from the $n_{H_2} \propto r^{-q}$ assumed profile.

From the continuum emission[6] at 219 GHz (0.5 pc×0.5 pc) and at 345 GHz (0.8 pc×0.8 pc) and the extent of the HC_3N $v = 0$ emission (see Figures 3 and 4), we modelled proto-SSC 13a up to a radius of 1.5 pc considering several density and temperature profiles.

4.3.1 *Non-local modelling results*

Figures 6 and 7 show the results for four representative models with star formation heating that best reproduce the continuum and the HC_3N* line emission. The models have an H_2 column density of $\sim 10^{25}$ cm^{-2} with two different density profiles ($q = 1$ and $q = 1.5$, modified as indicated above), and cover two different IR luminosities (L_{IR}) of 9.2×10^7 $L_\odot$ and 3.9×10^8 $L_\odot$. These luminosities are close to the protostar luminosity of 10^8 $L_\odot$ derived in Rico-Villas et al.

[6] Since the SSCs are being internally heated, the large column densities along with the greenhouse effect make the continuum emission to be much more intense at their center. Hence, the FWHMs do not reveal the total extension of the continuum emission.

Table 7. Parameters of the non-local radiative transfer models for the case of heating due to distributed star formation.

Model	q (pc)	L_{IR} ($L_\odot$)	Σ_{IR} ($L_\odot$ pc^{-2})	M_{H_2} ($M_\odot$)	L_{IR}/M_{H_2} ($L_\odot/M_\odot$)	r_e (pc)	N_{H_2} (cm^{-2})	N_{HC_3N} (cm^{-2})	χ^2_{lines}	Type
1	1.0	9.4×10^7	1.3×10^7	9.4×10^5	100	0.8	1.0×10^{25}	1.1×10^{18}	5.1	Dist.
2	1.5	9.4×10^7	1.3×10^7	9.5×10^5	99	0.4	1.2×10^{25}	3.1×10^{17}	4.5	Dist.
3	1.0	3.9×10^8	5.5×10^7	6.0×10^5	656	0.8	9.2×10^{24}	1.3×10^{17}	16.6	Dist.
4	1.5	3.9×10^8	5.5×10^7	6.1×10^5	638	0.4	1.0×10^{25}	9.7×10^{16}	11.0	Dist.
5	1.5	9.8×10^7	1.4×10^7	7.8×10^5	126	–	1.1×10^{25}	1.3×10^{17}	7.2	Central
6	1.0	9.8×10^7	1.4×10^7	9.0×10^5	109	–	1.0×10^{25}	1.3×10^{17}	10.9	Central
7	1.0	9.8×10^7	1.4×10^7	8.4×10^5	117	–	6.9×10^{24}	1.9×10^{17}	6.0	Central

Notes: All models have $r = 1.5$ pc. q is the power-law index assumed for the density profile. L_{IR} and Σ_{IR} are the luminosity and the luminosity surface density. M_{H_2} is the model total mass and L_{IR}/M_{H_2} the luminosity per unit of mass. r_e is the radius containing half of the star formation for distributed star formation models, which is $\propto n_{H_2} M_{H_2}$ for each shell (see González-Alfonso & Sakamoto 2019). For central star formation models, all the star formation is contained inside $r < 0.05$ pc. N_{H_2} and N_{HC_3N} are to the total H_2 and HC_3N column densities. χ^2_{lines} is the average of the $\chi^2_{line} = \sum_i \frac{(o_i - m_i)^2}{n\,\delta^2_{o_i}}$ for each line, where o_i and m_i are the observed and modelled line intensities, n the number of points taken into account, and δ_{o_i} is the observed error. Type refers to distributed or central star formation models.

(2020) for proto-SSC 13. A summary of the parameters of the most representative models, labelled 1 to 4, is shown in Table 7. Since we have corrected the model masses to fit the 235 GHz continuum emission in the outer regions (i.e. 0.85 − 1.5 pc), models with the same luminosity but different q index have similar final gas masses.

Figure 6 shows, in the upper left panel, the observed 235 GHz continuum emission at a $0.022'' \times 0.020''$ resolution (filled black circles) and the 345 GHz continuum emission at a $0.028'' \times 0.034''$ resolution (filled grey circles). The dashed lines represent the predicted continuum emission profiles of Model 2 ($q = 1.5$) at 235 GHz and 345 GHz for the corresponding T_{dust} profiles from González-Alfonso & Sakamoto (2019). The solid line show the continuum emission at 235 GHz derived from our modelling after varying X_d. Figure 6 also compares the modelled T_{dust} spatial profile considering the greenhouse effect for the different density profiles and luminosities. It also shows the HC_3N column density profiles (solid lines) with the values derived from `SLIM` in Section 4.2 (filled black circles) and the HC_3N abundance relative to H_2 ($X(HC_3N)$). Despite having similar H_2 column densities and/or L_{IR}, the difference in the density power-law index q ($q = 1.0$ or $q = 1.5$ for $n_{H_2} \propto r^{-q}$), translates into different H_2 densities and T_{dust} within a given shell, resulting in the different N_{HC_3N} and X_{HC_3N} profiles plotted in Figure 6. All models reproduce well the observed 235 GHz continuum emission, which, as expected, clearly shows that the models constrained only by dust emission are degenerated. Further constraints to the models are provided by considering the emission from the multiple detected HC_3N* lines as a function of the radius.

4.3.2 *Breaking the model degeneracy using HC_3N* emission*

Figure 7 shows the observed HC_3N* emission radial profiles at a resolution of $0.022'' \times 0.020''$ (filled black circles) and at a resolution of $0.028'' \times 0.034''$ (open circles) for the HC_3N* transitions listed in Table 5. The modelled HC_3N* radial profiles are also plotted at both resolutions with solid and dashed, respectively, colored lines for each model. Figure 7 shows that most lines from high vibrational excited states (high-energy lines) are well reproduced by the four models. Considering only these high-v lines, there is still a degeneracy between the considered models. Lowering T_{dust} (as in models 1 and 2, Fig. 6) decreases the emission of the high-energy transitions, which requires to significantly increase the HC_3N abundance in the hotter inner shells to reproduce the high-energy observed emission. Increasing n_{H_2} rises the HC_3N column density and therefore the HC_3N emission, which can be decreased by lowering its HC_3N abundance. However, we can favour one model over another by taking into account also the low-v lines (including the $v = 0$) and the physical constraints of the assumed model parameters.

4.3.3 *Model discrimination*

As already mentioned, the models are somewhat degenerated if only the continuum emission and/or very high-energy HC_3N* lines are considered, but one can break the degeneration by taking into account also the HC_3N lines arising from the $v = 0$ and $v_7 = 1$ states.

We propose to consider simultaneously both the high-energy and the low-energy transitions ratios to increase the dynamic range in energy. Such large energy range can be used thanks to the large number of HC_3N* transitions in the observed frequency range. We show in Figure 8 the ratio between the $v_7 = 1$ (24, 1 − 23, −1) and the $v_6 = 1$ (24, -1 − 23, 1) (i.e. $[v_7 = 1]/[v_6 = 1]$) as representative of the low-energy transitions and the ratio between the $v_6 = 1$ (24, -1 − 23, 1) and the $v_6 = v_7 = 1$ (26, 2, 2 − 25, −2, 2) (i.e. $[v_6 = 1]/[v_6 = v_7 = 1]$) as representative of the high-energy transitions. We can see that Model 3 and Model 4 fail to reproduce both line ratio profiles simultaneously. In the innermost region the $[v_6 = 1]/[v_6 = v_7 = 1]$ is close to the observed ratio but the $[v_7 = 1]/[v_6 = 1]$ ratio is far from being reproduced; the opposite effect is found for the $[v_7 = 1]/[v_6 = 1]$ ratio. On the other hand, Model 1 and Model 2 reproduce both ratios at the same time for all radii, with Model 2 predicting values closer to the observed ratios. Clearly, Models 3 and 4 grossly overestimate the emission of the low-energy $v = 0$ and $v_7 = 1$ from the innermost rings, while Models 1 and 2 agree much better with observations.

From the line integrated intensity radial profiles and from the $[v_7 = 1]/[v_6 = 1]$ and $[v_6 = 1]/[v_6 = v_7 = 1]$ line ratios profiles (Figures 7 and 8), Model 1 and Model 2 are the best in reproducing all spatial profiles (they have the lowest χ^2_{lines} values, see Table 7). These include the absorption features in the inner rings from the low-energy ground state $v = 0$ and $v_7 = 1$ transitions, and both line ratios. Between these two models, Model 2 is favored against Model

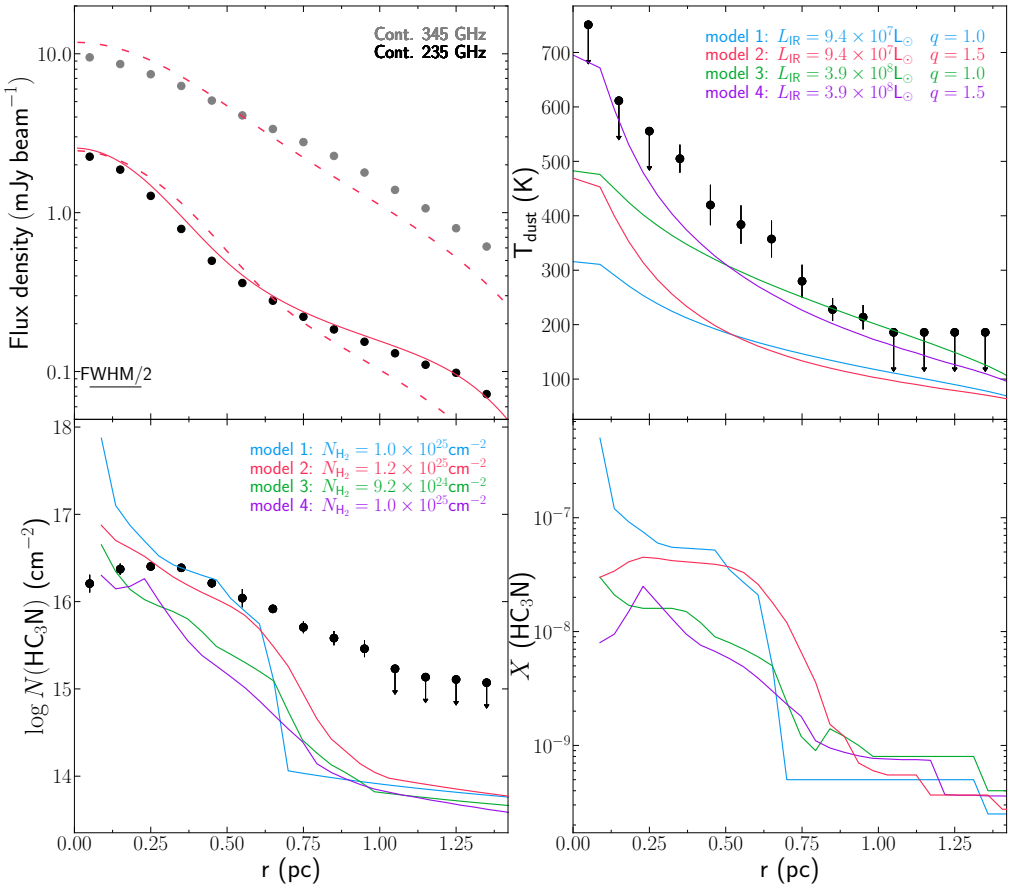

Figure 6. Observed and modelled continuum emission and parameters used each model (Model 1 in blue, Model 2 in red, Model 3 in green and Model 4 in purple) profiles. Upper left panel shows the rings continuum emission at 235 GHz with a resolution of $0.022'' \times 0.020''$ (black filled circles) and at 345 GHz at a resolution of $0.028'' \times 0.034''$ (grey filled circles). Dashed red lines show the continuum emission from Model 2 ($q = 1.5$) resulting from the T_{dust} profile for both frequencies, while the red solid line shows the continuum emission at 235 GHz resulting from the modelling after varying X_d to account for both the free-free emission in the innermost region and the excess of continuum emission in the outermost region. Upper right and lower left panels show the dust temperature ($\sim T_{vib}$) and column density profiles obtained from the SLIM LTE model (black filled circles) for the averaged ring spectra and the solid colored lines indicates the profiles of each non-local model. Lower right panel solid colored lines show the HC$_3$N abundance profiles for each model. Half of the beam FWHM (i.e. 0.011″) is shown on the upper right panel.

1 because Model 2 reproduces better the $[v_7 = 1]/[v_6 = 1]$ and $[v_6 = 1]/[v_6 = v_7 = 1]$ line ratios. Also, for Model 1, the $v = 0$ line is not reproduced. Even Model 2, while showing a stronger decrease in the $v = 0$ flux towards the center, still cannot fully reproduce it, suggesting that the HC$_3$N column density towards the innermost rings is somewhat higher than in the model. Moreover, Model 1 requires a rather "strange" HC$_3$N abundance profile (with very high abundances towards the center, see Figure 6) in order to reproduce the distributions of the high-energy lines.

In summary, assuming spherical symmetry with a temperature and density radial profiles obtained in a consistent way considering the heating from the greenhouse effect due to the large optical depths in the IR and distributed star formation heating, Model 2 is able to reproduce the radial distribution of the continuum and the HC$_3$N* emission.

5 DISCUSSION

5.1 Dust temperature profiles derived from local and non-local radiative transfer analysis

If we compare the T_{dust} and the N(HC$_3$N) profiles derived from Model 2, which take into account non-local radiative transfer effects, with those derived from the SLIM LTE analysis, we can see very significant differences in both profiles (see Fig. 6). The differences in the dust temperature (overall higher T_{dust} values for the SLIM model) arise from the fact that the SLIM LTE model does not include non-local radiative transfer effects along the line of sight, which are crucial for the large column densities, H_2 density and dust temperature profiles expected in the very early phases of the SSCs formation. These effects give rise to the absorption features in the inner regions for the lines of the low $v = 0$ and $v_7 = 1$ vibrational states, which decrease their intensities in relation to higher-v transitions, indicating that lines from different vibrational states arise from different regions and thus sample different physical conditions along the line of sight. When these transitions are not taken into account to avoid this effect, as considered for the SLIM model inner regions, the covered energy range is reduced and the SLIM fit tends to rise T_{dust} as

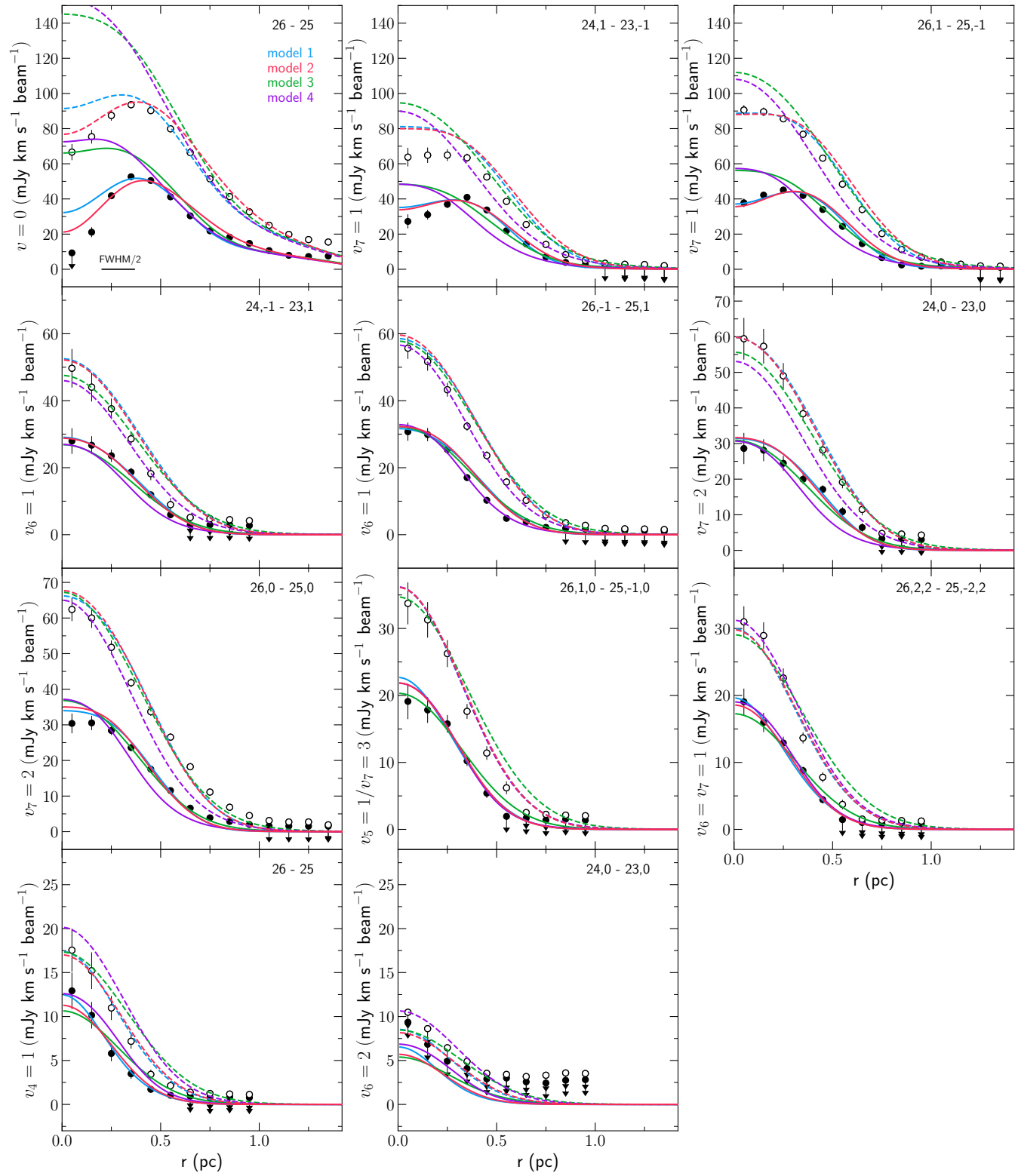

Figure 7. Observed and modelled HC_3N* line emission spatial profiles of the transitions listed in Table 5. Black filled and open circles show the integrated line intensity of the averaged ring spectra at $0.022'' \times 0.020''$ and $0.028'' \times 0.034''$ resolution, respectively, for each HC_3N* transition (quantum number of the transition are indicated on the upper right corner of each panel). Colored lines show the modelled emission for each model (Model 1 in blue, Model 2 in red, Model 3 in green and Model 4 in purple) at a resolution of $0.022'' \times 0.020''$ (solid lines) and $0.028'' \times 0.034''$ (dashed lines). Half of the beam FWHM is shown on the first panel.

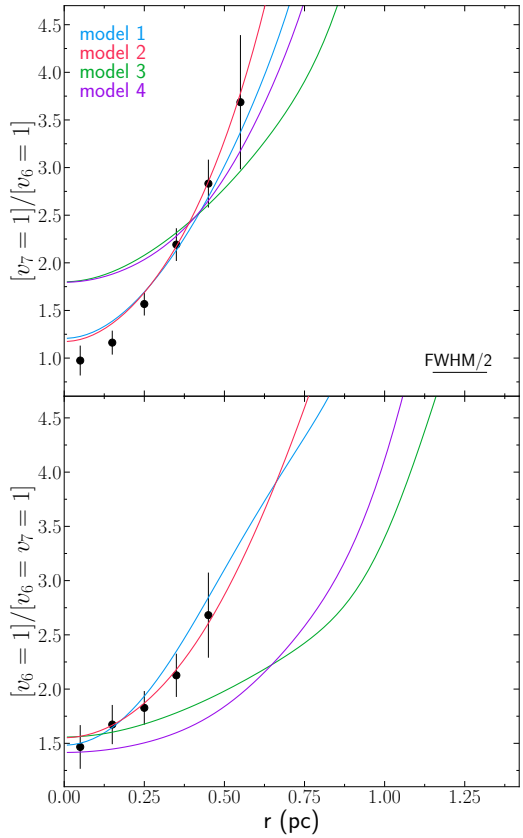

Figure 8. Observed and modelled HC_3N* line ratios radial profiles. Left panel shows the ratio between the $v_7 = 1$ (24, 1 − 23, −1) and the $v_6 = 1$ (24, −1 − 23, 1) transitions. Right right panel shows the ratio between the $v_6 = 1$ (24, −1 − 23, 1) and the $v_6 = v_7 = 1$ (26, 2, 2 − 25, −2, 2) transitions.

the absorption also affects the $v_7 = 2$ and $v_6 = 1$, although to a lesser extent than for the $v = 0$ and $v_7 = 1$. Even at large radii, the LTE dust temperature is overestimated. This is due to the combination of different optical depths in the $v = 0$ and the $v_7 = 1$ lines and the $T_{\rm dust}$ radial gradient, making both lines to trace the region where they become optically thick and therefore tracing different $T_{\rm dust}$ within the proto-SSC. Since the $v = 0$ lines are optically thick at larger radii where the $v_7 = 1$ lines are optically thin, the $T_{\rm dust}$ traced by the $v = 0$ lines will be smaller than that from the $v_7 = 1$ lines. This effect will also appear for any pair of lines from different vibrationally excited levels. Also, since the rings width is smaller (0.1 pc) than half of the beam FWHM (0.17 pc), which is the true resolution power of the observations, each ring has also a contribution from the adjacent rings in the sky plane, however we expect it to affect to a lesser extent the differences in the $T_{\rm dusts}$ profile than the contribution from other rings along the line of sight. Regarding the HC_3N column density, its profile is similar at small radii to that of the non-local models, but at longer radii (> 0.7 pc) they start to differ significantly. This is partially due to subthermal excitation (difference between $T_{\rm rot}$ and $T_{\rm vib}$) found in Costagliola & Aalto (2010) and Rico-Villas et al. (2021), which tends to overestimate the LTE HC_3N column densities when considering $T_{\rm vib}$, instead of $T_{\rm rot}$, for the calculation in `SLIM`. Observations of less abundant isotopologues will help to alleviate the optical depth problems in the LTE analysis. Unfortunately, the isotopologues lines are weaker and the potential lines to be detected in extragalactic sources will be limited to the lines arising from the lowest vibrational levels.

5.2 Central vs. distributed star formation

The models described above assume that the star formation spatial profile is proportional to the gas density and mass, injecting energy from stars at different radii. The energy deposition per unit of time and volume is proportional to the SFR per unit of volume (see González-Alfonso & Sakamoto 2019, for details). This is reflected in the different $T_{\rm dust}$ profiles for a given column density and power-law index q. Consequently, a $q = 1.0$ index represents a more scattered star formation than a $q = 1.5$ index, as illustrated by r_e, the radius that contains half of the star formation (i.e. luminosity). Models with $q = 1.0$ have a more extended r_e of ∼ 0.8 pc and models with $q = 1.5$ a smaller r_e ∼ 0.4 pc. The selected model, i.e. Model 2, has a $q = 1.5$ (r_e ∼ 0.4 pc), indicating that a higher concentration of star formation (or the most massive stars) is located at the center of proto-SSC 13a, although a fraction of the star formation also takes place at larger radii.

To test the assumption of distributed star formation in the proto-SSC 13a, we have also modelled the HC_3N* and continuum emission assuming that the star formation only takes place in the very central region (∼ 0.05 pc, i.e. central star formation). To do so, we have used the "AGN" model profiles for $T_{\rm dust}$ from González-Alfonso & Sakamoto (2019). Figure 9 compares the distributed star formation Model 2 with three central star formation models (Models 5, 6 and 7). The three models have the same luminosity as Model 2 ($L_{\rm IR} = 9.2 \times 10^7\,{\rm L}_\odot$), and Models 5 and 6 also the same column density ($N_{\rm H_2} = 10^{25}\,{\rm cm}^{-2}$), but Model 7 has a lower column density ($N_{\rm H_2} = 5.6 \times 10^{24}\,{\rm cm}^{-2}$). For the same luminosity and column density as the models with distributed star formation from Section 4.3, the central star formation models have much steeper $T_{\rm dust}$ profiles. Due to the small size of the region forming stars of ∼ 0.05 pc located in the center, the greenhouse effect makes radiation to escape more difficult than if star formation were distributed all over the source for the same dust column density. In the outermost regions, however, the central and distributed star formation models have similar dust temperatures.

Central star formation models suffer similar problems as Models 3 and 4: the high temperature in the central region boosts too much the high-energy transitions, requiring lower abundances than Model 2. To compensate this, we lower the column density to $5.6 \times 10^{24}\,{\rm cm}^{-2}$ in Model 7, which allows to maintain similar abundances as in Model 2. However, lowering the column densities reduces the absorption effect of Model 2, so that Models 5, 6 and 7 strongly overestimate the emission of the low-energy lines (mostly the $v = 0$). Figure 10 shows the comparison of the low-energy $[v_7 = 1]/[v_6 = 1]$ line ratio and the high-energy $[v_6 = 1]/[v_6 = v_7 = 1]$ line ratio between these models. Model 7, despite reproducing well the $[v_6 = 1]/[v_6 = v_7 = 1]$ ratio, fails to reproduce the low-energy $[v_7 = 1]/[v_6 = 1]$ as it underestimates the $v_6 = 1$ (24, −1 − 23, 1) emission at $r > 0.1$ pc and with its lower column density is unable to reproduce the absorption observed in the $v_7 = 1$ and $v = 0$ line profiles.

All the temperature profiles from our modelling show that massive star formation is concentrated in the central region of proto-SSC 13a. However, we have discarded Model 7 (the best model with only star formation at the center), since it does not reproduce simultaneously the low-energy line profiles and the $[v_6 = 1]/[v_6 = v_7 = 1]$ line ratio. For models with distributed star formation, Model 2 best matches the observations and both line ratios. Therefore, our modelling indicates that the most massive star formation is taking place in the central region of proto-SSC 13a (with r_e ∼ 0.4 pc), but star formation is distributed over a more extended region (∼ 80% of the star formation takes place inside $r = 0.9$ pc).

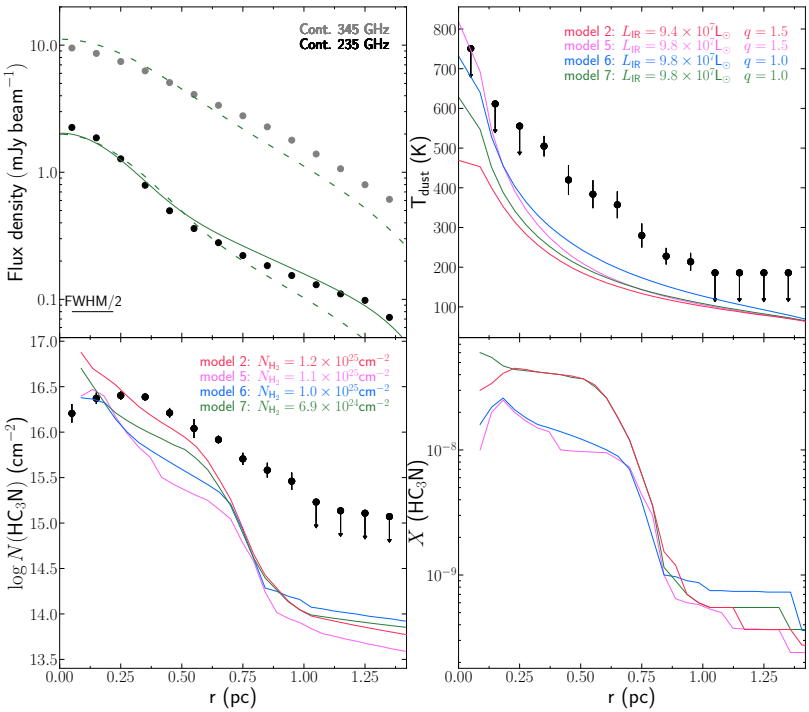

Figure 9. Same as Figure 6 but for the spatially distributed star formation Model 2 (in red), and the central star formation Model 5 (in magenta), Model 6 (in dark blue) and Model 7 (in dark green), see Section 5.2.

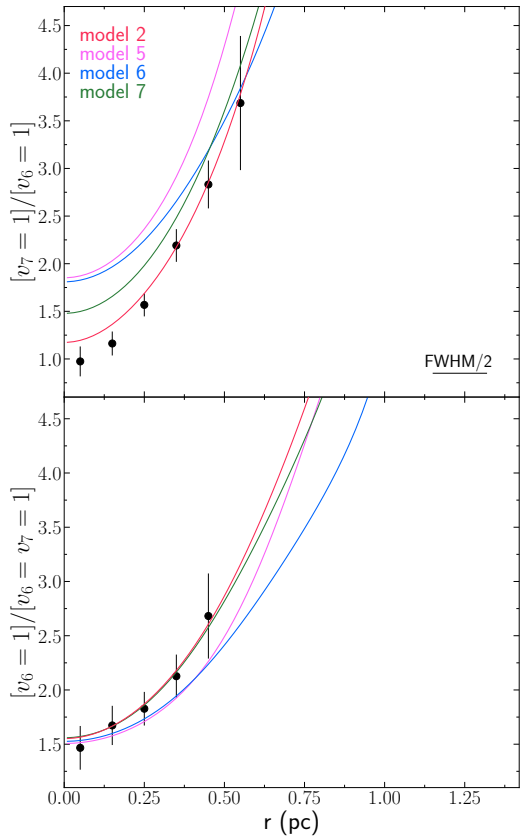

Figure 10. Same as Figure 8 but with Model 2 (in red), Model 5 (in magenta), Model 6 (in dark blue) and Model 7 (in dark green).

5.3 Star formation scenarios

A centrally peaked but distributed star formation would be in accordance with the competitive accretion scenario, where most massive stars are being formed at the center of cluster potential well and less massive stars at the outskirts (e.g. Bonnell et al. 1997, 2001; Murray & Chang 2012). Also, this would mean that mass segregation (i.e. the most massive stars in the center of a star cluster) observed in more evolved SSCs (Bonnell et al. 2001, 2007) is already set in place at the early ages of proto-SSC 13a ($t_{age} \sim 4 \times 10^4$ yr, see Rico-Villas et al. 2020) as the competitive accretion naturally predicts. Furthermore, it has also been suggested that primordial mass segregation is present in the star clusters of the Milky Way (less massive than SSCs; e.g. McMillan et al. 2007; Pavlík et al. 2019) or in the much older (and comparable in mass to SSCs) globular clusters of the Milky Way with typical half-light radii of ~ 3 pc (e.g. Haghi et al. 2014).

5.4 The proto-SSC 13a velocity structure: cloud-cloud induced star formation

From the 2D analysis of the HC$_3$N* emission in Section 4.1 we have seen that there is a velocity structure in proto-SSC 13a that can provide information on the triggering process of the formation of SSCs. We find a separation of ~ 21 km s^{-1} between the minimum (242 km s^{-1}) and maximum (263 km s^{-1}) velocities in proto-SSC 13a. Here we briefly discuss three possible origins: rotation, outflow or cloud-cloud collision.

We can discard that the cloud is rotating. Figure 4 shows that the local velocity change occurs in the southeast-northwest (SE-NW) direction, just perpendicular to the rotation of the galaxy disk in the northeast-southwest (NE-SW) direction. Such rotation pattern would be hard to explain in the context of the NGC 253 disk kinematics and the conservation of angular momentum. Furthermore, in Figure 4 we

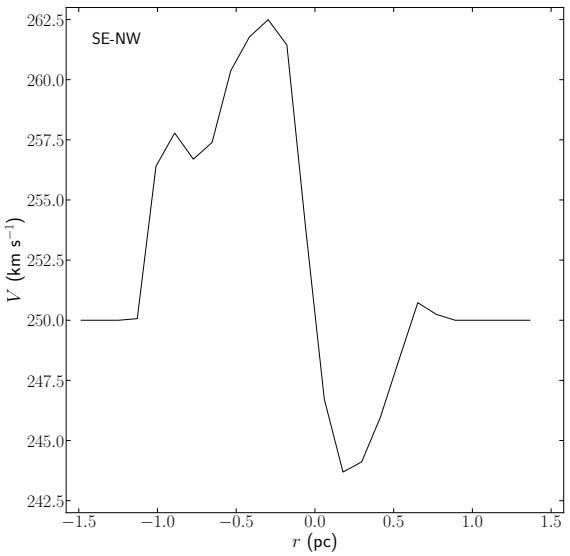

Figure 11. Proto-SSC 13a velocity profiles derived from the SLIM fitted values in the southeast-northwest direction (i.e. perpendicular to the galaxy rotation plane) in the left panel and in the northeast-southwest direction (i.e. parallel to the galaxy rotation plane) in the right panel.

can see that the region with larger velocities ($250 - 263\,\mathrm{km\,s^{-1}}$) is extended towards the northeast and also surrounds the region with lower velocities ($243 - 250\,\mathrm{km\,s^{-1}}$) on the west, difficult to match with a rotation pattern. Figure 11 shows the velocity profile through the local velocity change (i.e. the SE-NW direction). It can be seen that there are two differentiated regions with different velocities: a larger cloud with velocities going from $\sim 263 - 250\,\mathrm{km\,s^{-1}}$ and a smaller cloud with $\sim 250 - 242\,\mathrm{km\,s^{-1}}$.

If the local velocity change is caused by outflowing gas, we should see the characteristic P-Cygni profiles in some of the observed transitions, or at least line wings in the spectra of the lowest-energy lines. However, we do not observe such features despite the large column densities present in proto-SSC 13a. Also, as indicated by Levy et al. (2021), some vibrationally excited emission lines are coincident with the blueshifted absorption (in our case the $v_5 = 1/v_7 = 3$ line is coincident with the $v = 0$ line) could help to conceal the P-Cygni profiles. Because of this, Levy et al. (2021) do not observe clear P-Cygni profiles for SSC 13a in their study of the CS 7 – 6 and $H^{13}CN$ 4 – 3 transitions, as they do for SSCs 4a, 5a and 14.

Since the outflow cannot be completely ruled out, we estimate some of its properties. We consider that the systemic velocity of the SSC is $250\,\mathrm{km\,s^{-1}}$ and the gas is outflowing with a projected velocity of $10 - 15\,\mathrm{km\,s^{-1}}$. Note that the outflow terminal velocity would be larger since the outflow might not be along the line of sight. Assuming a 45° inclination, the terminal velocity would be about $20\,\mathrm{km\,s^{-1}}$. We can derive the mass of the outflowing small cloud with velocities $< 250\,\mathrm{km\,s^{-1}}$ from the total gas mass ($M_{H_2} = 9.5 \times 10^5\,M_\odot$) and density profile ($n_{H_2} \propto r^{-1.5}$) obtained in Section 4.3.3 for Model 2. The outflowing mass for the blueshifted cloud with $< 250\,\mathrm{km\,s^{-1}}$ would be $M_{\mathrm{out},H_2} \sim 7 \times 10^4\,M_\odot$. Unfortunately, the estimate of the mass of the redshifted cloud is more complicated, since it merges with the ambient gas which is not expected to be participating in the outflow. We thus guess that it has a similar mass that the blueshifted gas. We can also estimate the dynamical age of the outflow by considering the distance of the outflowing cloud to its origin and the terminal velocity ($\delta v = 21\,\mathrm{km\,s^{-1}}$). For a distance of ~ 0.2 pc (i.e. the position of the blueshifted cloud from the expected origin) we obtain a dynamical age $t_{dyn} \sim 10^4$ yr. With these parameters we estimate its momentum flux by $\dot{P}_{out} = \dot{M}_{out}\delta v = 9.3 \times 10^{32}\,\mathrm{g\,cm\,s^{-2}}$, where $\dot{M}_{out} = M_{\mathrm{out},H_2}/t_{dyn}$. If we consider that the outflow is only driven by radiation, $\dot{P}_{out}$ should be compatible with $\sim L_{IR}/c = 1.3 \times 10^{31}\,\mathrm{g\,cm\,s^{-2}}$ (see Murray et al. 2005), which is not the case. The latter and the lack of observed P-Cygni profiles, are in agreement with the idea that proto-SSC 13a is very young and where very likely the mechanical feedback from stars is not yet affecting significantly its gas content.

We now consider the possibility of a cloud-cloud collision in which the gas with velocities $\sim 242 - 250\,\mathrm{km\,s^{-1}}$ would be in a cloud of $7 \times 10^4\,M_\odot$ which is driving into a larger cloud of $8.8 \times 10^5\,M_\odot$ with velocities $\sim 250 - 263\,\mathrm{km\,s^{-1}}$. The velocity of the small colliding cloud is also consistent with the non-disk component identified in the study of NGC 253 kinematics from CO emission by Krieger et al. (2019). This scenario also fits within the observed velocity structure shown in Figures 4, with the smaller cloud being surrounded by the large cloud which still maintains its velocities, and is similar to what is expected in the early stages of a cloud-cloud collision (e.g. Habe & Ohta 1992; Takahira et al. 2014; Haworth et al. 2015). At the collision front, a dense layer of material is developed as the small cloud advances through the large cloud, inducing the formation of gravitationally unstable cores that lead to massive star formation (Inoue & Fukui 2013). Such external triggering of massive star formation has been invoked for the formation of several young massive clusters (YMCs) of the Milky Way and of the Large Magallanic Cloud (e.g. Furukawa et al. 2009; Ohama et al. 2010; Fukui et al. 2016, 2018; Fujita et al. 2021; Tsuge et al. 2021).

The compressed interface layer between the two clouds is usually translated into a region with intermediate velocities connecting the two clouds (i.e. a bridge feature) separated in velocity (but not spatially) in a position-velocity diagram (hereafter p-v diagram) like those shown in Figure 12. In the HC_3N column density p-v diagram (Figure 12 left panel) we can see the bridge feature with intermediate velocities connecting the two colliding clouds separated in velocities. However, in the p-v diagram of the vibrational temperature (Figure 12 right panel), the bridge feature is less clear and no clear pattern of the highest temperatures, which one would expect to be located in the bridge feature, is observed. Still, the overall velocity structure seems to favour the cloud-cloud collision scenario rather than the outflow.

5.5 Derived properties for Proto-SSC 13a

The derived radius of 1.5 pc for proto-SSC 13a is close to the smallest observed SSCs, which have typical radius between 1 and 5 pc. From Model 2, we obtain for proto-SSC 13a a luminosity of $L_{IR} = 9.4 \times 10^7\,L_\odot$, a luminosity surface density of $1.3 \times 10^7\,L_\odot\,\mathrm{pc^{-2}}$, and a molecular gas mass of $M_{H_2} = 9.5 \times 10^5\,M_\odot$ (see Table 7).

5.5.1 SSC formation through rapid collapse

From the total gas mass obtained for proto-SSC 13a we can derive its virial parameter $\alpha = 5\sigma^2 R/GM_{H_2}$, where σ is the velocity dispersion. From the mean of all the fitted FWHMs for each pixel in Section 4.1 ($\sim 25\,\mathrm{km\,s^{-1}}$) we obtain a mean $\bar{\sigma} \sim 11\,\mathrm{km\,s^{-1}}$. Using this $\bar{\sigma}$, the virial parameter is $\alpha \approx 0.21$, well below the value of 2 to consider the cloud to be bounded and thus being supercritical. If we take into account the derived density profile in the innermost region ($n_{H_2} \propto r^{-1.5}$), α would be even smaller (Kauffmann et al. 2013). In this supercritical state ($\alpha \ll 2$), proto-SSC 13a would be

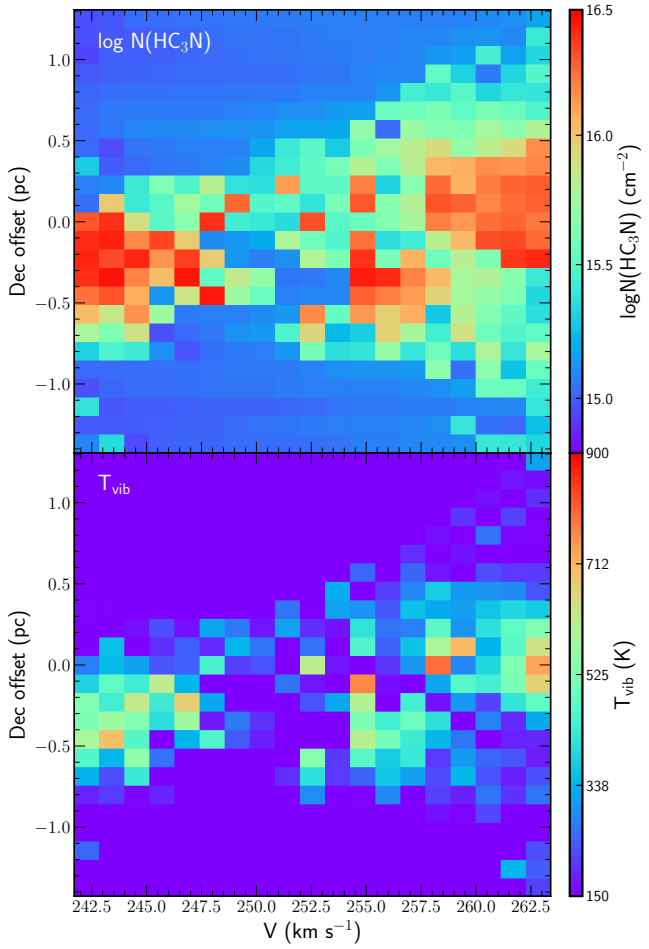

Figure 12. Proto-SSC 13a position velocity diagrams of the HC_3N column density (top panel) and the vibrational temperature (bottom panel) derived with `SLIM`.

unstable and indicates a rapid collapse. Such a low virial parameter is typically found in high-mass star forming clumps and cores (see Kauffmann et al. 2013, for a review on regions with supercritical virial parameters).

We now investigate if the radiation pressure from the forming stars can disperse or at least halt the collapsing natal material of proto-SSC 13a. From González-Alfonso & Sakamoto (2019), the Eddington flux can be derived from $F_{\rm Edd} = \Psi_{\rm th}\Sigma_{\rm H_2}/(1-\Psi_{\rm th}/\Psi)$, where $\Sigma_{\rm H_2}$ is the gas surface density, Ψ the light-to-mass ratio of the current stellar population and $\Psi_{\rm th}$ is the light-to-mass ratio threshold value given by

$$\Psi_{\rm th} = \frac{4\pi G c}{\kappa_{\rm F}} = 1.3\times10^3 \left(\frac{\kappa_{\rm F}}{10{\rm cm^2\,g^{-1}}}\right)^{-1} {\rm L_\odot\,M_\odot^{-1}}, \quad (1)$$

with $\kappa_{\rm F}$ the Rosseland mean opacity. Assuming $\kappa_{\rm F}$ to be $10\,{\rm cm^2\,g^{-1}}$ (typical for a hot starburst with $T > 200$ K, see Andrews & Thompson 2011), $\Psi_{\rm th} = 1.3\times10^3\,{\rm L_\odot\,M_\odot^{-1}}$. If $\Psi < \Psi_{\rm th}$, gravity overcomes the radiation pressure and the cloud can collapse further. For a model with $N_{\rm H_2} = 10^{25}\,{\rm cm^{-2}}$, $\Sigma_{\rm IR} = 1.1\times10^8\,{\rm L_\odot\,pc^{-2}}$, González-Alfonso & Sakamoto (2019) shows that the outward force due to radiation pressure (red curve in panel b of their Figure 6) is close to the inward gravity force (green lines in panel b of their Figure 6) only in the innermost regions, with gravity overcoming radiation pressure in the external regions, even for a large Ψ of $1700\,{\rm L_\odot\,M_\odot^{-1}}$. Given that $\Sigma_{\rm IR}$ for proto-SSC 13a is lower, gravity would overcome radiation pressure more easily. Also, we can make a simpler estimation of the Eddington luminosity for proto-SSC 13a from $L_{\rm Edd} = 4\pi cGM/\kappa_F$, which results in $10^9\,{\rm L_\odot}$, an order of magnitude larger than the derived $L_{\rm IR}$. From the above calculations, we conclude that the radiation pressure is not able to overcome gravity and prevent proto-SSC 13a from collapse.

5.5.2 *Short timescales and high SFE*

Since proto-SSC 13a is collapsing, we can estimate its free-fall time from $t_{\rm ff} = \sqrt{3\pi/(32{\rm G}\bar{\rho})}$, where $\bar{\rho}$ indicates the mean gas density. For proto-SSC 13a, $\bar{\rho} = 4.5\times10^{-18}\,{\rm g\,cm^{-3}}$, which gives a free-fall time $t_{\rm ff} = 3\times10^4$ yr, very similar to its estimated age ($t_{\rm age} \sim 4\times10^4$ yr) in Rico-Villas et al. (2020). The small α and a $t_{\rm ff} \sim t_{\rm age} \sim 10^4$ yr indicate that proto-SSC 13a has just started to form stars and that it is doing so very rapidly. This would be in accordance with the lack of detection of outflow signatures, which would not have had enough time to develop and/or alter the gas content.

Therefore, if we consider that no mechanical feedback is taking place and there has not been gas ejection, we can estimate the star formation efficiency (SFE) as in Rico-Villas et al. (2020)

$${\rm SFE} \sim \frac{1}{1 + M_{\rm H_2}/(M_{\rm p*} + M_*)}, \quad (2)$$

where M_* is the ZAMS stellar mass derived by Leroy et al. (2018) from the 36 GHz continuum emission and assuming a light-to-mass ratio of $10^3\,{\rm L_\odot\,M_\odot^{-1}}$ ($M_* = 6.3\times10^4\,{\rm M_\odot}$, see Rico-Villas et al. (2020)), and $M_{\rm p*}$ is the protostellar mass derived from $L_{\rm IR}$ and assuming the same light-to-mass ratio ($M_{\rm p*} = 9.4\times10^4\,{\rm M_\odot}$). The resulting SFE is ~ 0.14 (0.09 if only the protostars were accounted for). The value is lower than that obtained in Rico-Villas et al. (2020) since with the more detailed modelling of high-v HC_3N* transitions we estimate a higher gas content. Despite the youth of proto-SSC 13a, it has already been able to convert $\sim$ 14% of its gas content in stars with an "instantaneous" star formation rate (in a free-fall time) SFR= $5\,{\rm M_\odot\,yr^{-1}}$ ($3\,{\rm M_\odot\,yr^{-1}}$ taking into account only the protostars being formed). Given the derived SFR, the time to consume all the gas content ($t_{\rm dep}$) would be 2×10^5 yr. This $t_{\rm dep}$ is close to the timescale for cluster formation of $5t_{\rm ff}$ found by Skinner & Ostriker (2015) in their simulations. If we assume a more conservative final SFE of 0.5, the time to convert the 50% of the remaining gas mass into stars is $\sim 7\times10^4$ yr, on the order of $3t_{\rm ff}$.

The high SFR ($3-5\,{\rm M_\odot\,yr^{-1}}$) derived for the individual proto-SSC 13a (and also for the remaining SSCs seen in Rico-Villas et al. (2020)) contrasts with the low SFR if derived from the IR luminosity following the relation given by Kennicutt (1998) (and other similar relations) of SFR= $4.5\times10^{-44}L_{\rm IR}({\rm erg\,s^{-1}}) \approx 0.01\,{\rm M_\odot\,yr^{-1}}$. This is because these relations are meant for entire galaxies and therefore, in order to calibrate their SFR-$L_{\rm IR}$ relation, they assume continuous star formation over $(10-100)\times10^6$ yr. These large timescales are not comparable to the young ages of the SSCs forming stars in NGC 253 much shorter ($(1-10)\times10^4$ yr) timescales. Hence, the SFRs we derive in Rico-Villas et al. (2020) and in this paper can be understood as an instantaneous SFR. In fact, the factor $\sim$ 300 between the SFR derived in this paper and that from the relation given by Kennicutt (1998), is similar to the factor between the different timescales considered of 3×10^4 yr and 10^7 yr.

5.5.3 *Triggering the SSC formation*

It has been suggested that the formation of SSCs involve a rapid collapse and enhanced SFE, requiring extreme external pressures of $P_e/k \gtrsim 10^8\,\mathrm{K\,cm^{-3}}$ (Elmegreen & Efremov 1997). Following Johnson et al. (2015) and Finn et al. (2019), the external pressure confining the cloud mass to the observed radius, given its velocity dispersion, can be obtained from

$$P_e = \rho_e \sigma^2 = \frac{3\Pi M \sigma^2}{4\pi r^3}, \quad (3)$$

where $\rho_e = \Pi\bar{\rho}$ is the density at the edge of the cloud and where we use the same 0.5 value for Π as Johnson et al. (2015) to estimate the density at the cloud's edge from the average cloud density $\bar{\rho}$. For proto-SSC 13a we obtain $P_e/k = 1.8 \times 10^{10}\,\mathrm{K\,cm^{-2}}$, two order of magnitudes greater than the required external pressure to avoid the dispersal of the forming SSC gas. But what is driving such a high external pressure? As discussed in Section 5.2, the velocity structure matches with a cloud-cloud collision. Such a mechanism could increase the pressure in proto-SSC 13a to the observed values. A rough estimation of the ram pressure induced by the collision of the two colliding clouds separated by $21\,\mathrm{km\,s^{-1}}$ is given by $P = \bar{\rho}v^2$ (Finn et al. 2019), which results in $P/k \sim 10^{11}\,\mathrm{K\,cm^{-3}}$ and shows that the cloud-cloud collision is able to provide the observed high external pressure to support SSCs formation.

5.6 Comparison to other buried star forming regions

Due to the deeply buried nature of proto-SSC 13a in the SHC phase, we can compare the results obtained for proto-SSC 13a with similar embedded sources. On the lower luminosity end, we can compare the SHC phase in proto-SSC 13a to the Milky Way HCs. In fact, the SHC phase observed in proto-SSC 13a seems to be a scaled-up version of Milky Way HCs. HCs, with luminosities $\lesssim 10^7\,\mathrm{L_\odot}$, are heated by a few massive protostars in a small cluster. In order to compare to proto-SSC 13a, we selected the HCs sample from Rolffs et al. (2011) (see Table 8) since they derive their masses in a similar fashion as in our radiative transfer modelling (Section 4.3), taking into account the high opacity at the center of HCs and modelling the continuum emission accordingly (i.e. including the trapping of radiation or greenhouse effect) together with the emission from vibrationally excited HCN. We use the IRAS luminosities and the FWHMs from the ATLASGAL survey at 870 µm (345 GHz) listed in Rolffs et al. (2011) Table 1 (see references therein). Additionally, for SgrB2(M) and SgrB2(N) HCs, we also use the values derived by Etxaluze et al. (2013) from Herschel observations. On the higher luminosity end, we have the highly obscured nuclear regions of (U)LIRGs. These buried galactic nuclei (hereafter BGNs; also known as CONs, Falstad et al. 2021) have large column densities ($N_{\mathrm{H_2}} > 10^{24}\,\mathrm{cm^{-2}}$) that span through the compact nuclear region ($\lesssim 100\,\mathrm{pc}$) with very high luminosities ($L_{\mathrm{IR}} \gtrsim 10^{11}\,\mathrm{L_\odot}$) powered by a starburst and/or an AGN. The BGNs parameters listed in Table 8 are taken from González-Alfonso & Sakamoto (2019) and the masses from González-Alfonso et al. (2015) (see also references therein). For most sources, different values of R and L_{IR} are given, reflecting the uncertainty in their estimation.

Due to the large difference, of several orders of magnitude, in radii, luminosities and masses between HCs and BGNs, we normalize these quantities by their size or by their gas mass to facilitate the comparison. Therefore, we estimate the luminosity surface density $\Sigma_{\mathrm{IR}} = L_{\mathrm{IR}}/(\pi r^2)$, mass surface density $\Sigma_{\mathrm{H_2}} = M_{\mathrm{H_2}}/(\pi r^2)$, and the luminosity per unit gas mass $L_{\mathrm{IR}}/M_{\mathrm{H_2}}$. The latter can be considered a proxy of the star formation efficiency as the derived luminosity arises from the embedded (proto)stars at the stage of SHC in which proto-SSC 13a is at (see Rico-Villas et al. 2020). For proto-SSC 13a these values, from Model 2, are: $\Sigma_{\mathrm{IR}} = 1.3 \times 10^7\,\mathrm{L_\odot\,pc^{-2}}$, $\Sigma_{\mathrm{H_2}} = 1.3 \times 10^5\,\mathrm{M_\odot\,pc^{-2}}$, and $L_{\mathrm{IR}}/M_{\mathrm{H_2}} = 99\,\mathrm{L_\odot\,M_\odot^{-1}}$.

In Figure 13 we compare the properties of BGNs and Milky Way HCs with proto-SSC 13a in between. The upper left panel shows the luminosity surface density versus the squared radii of the sources. It can be seen that proto-SSC 13a has an intermediate luminosity, at least one order of magnitude larger than HCs, but a size similar to the largest HCs. On the other hand, BGNs have much larger luminosities (three orders of magnitude larger than SHC 13a) and also larger radii. On the right panel we plot the luminosity surface density now compared to the surface mass density. It can be seen that there is a trend with higher Σ_{IR} for larger $\Sigma_{\mathrm{H_2}}$, but for HCs and the proto-SSC 13a the $L_{\mathrm{IR}}/M_{\mathrm{H_2}}$ ratio is $\lesssim 100$ (lower panels). This would point to a limit on the amount of mass per surface area that embedded star formation can heat to produce the observed Σ_{IR}.

A similar trend is found in the lower left and right panels of Figure 13, where $L_{\mathrm{IR}}/M_{\mathrm{H_2}}$ increases as the mass and the luminosity surface increase, but staying $\lesssim 100$ for HCs and proto-SSC 13a. For the latter, this would indicate the star formation proceeds much more efficiently than in most HCs (higher $L_{\mathrm{IR}}/M_{\mathrm{H_2}}$), close to the limit to what is observed in non-interacting or weakly-interacting star-forming galaxies (Solomon & Sage 1988; Gao & Solomon 2004; Graciá-Carpio et al. 2011). Instead, strong interacting or merging galaxies, like those hosting the BGNs, have $L_{\mathrm{IR}}/M_{\mathrm{H_2}} \gtrsim 100$ (indeed they are located above the dashed lines in Figure 13). It has been proposed that this is due to a different mode of star formation, in which BGNs (i.e. (U)LIRGs) are able to convert an extraordinary amount of gas in extremely short times and in a very efficient manner (remember that $L_{\mathrm{IR}}/M_{\mathrm{H_2}}$ can be considered as a proxy to SFE) despite the probable presence of an AGN. We propose that, since massive star formation in HCs and proto-SSCs is already taking place very efficiently (Rico-Villas et al. 2020), and that for the latter it does so in a very rapid and vigorous way, the excess of $L_{\mathrm{IR}}/M_{\mathrm{H_2}}$ above $\sim 100\,\mathrm{L_\odot\,M_\odot^{-1}}$ probably arises from the contribution of a buried AGN. However, the analysis of the remaining SSCs observed in NGC 253 is required to confirm this hypothesis.

6 CONCLUSIONS

With very high resolution ALMA observations ($0.022'' \times 0.020'' \approx 0.37\,\mathrm{pc} \times 0.34\,\mathrm{pc}$) at 219 GHz, we have resolved the young SSCs studied in Rico-Villas et al. (2020). Fragmentation is observed in most of them. Due to its unique properties, we have focused on the study of the HC_3N^* emission of proto-SSC 13a because it is one of the brightest sources at 219 GHz and 345 GHz, it appears to have a circular symmetry around the center, and was already classified among the youngest proto-SSCs in Rico-Villas et al. (2020). Our main results for proto-SSC 13a can be summarized as follows:

(1) The spectra shows the typically abundant molecular line emission observed towards HCs in the Milky Way. We have detected many rotational $J = 24-23$ and $J = 26-25$ HC_3N transitions from highly vibrationally excited states, covering a wide energy range from 131 K up to 1399 K.

(2) Using the `SLIM` module within MADCUBA, we have carried out a 2D LTE analysis of the excitation of HC_3N^*, obtaining maps of the HC_3N column density, vibrational temperature (T_{vib}), velocity and FWHMs. From the temperature map, we identify a small region

Table 8. Parameters of HCs (from Rolffs et al. 2011), proto-SSC 13 (this work) and BGNs (from González-Alfonso et al. 2015; González-Alfonso & Sakamoto 2019)

HC Source	D (kpc)	R (pc)	L_{IR} (10^5 $L_\odot$)	Σ_{IR} (10^5 $L_\odot$ pc^{-2})	M_{H_2} (10^3 $M_\odot$)	L_{IR}/M_{H_2} ($L_\odot/M_\odot$)
IRAS12326-6245	4.4	0.57	2.7	2.7	4.2	64
G327.3-06	2.9	0.39	1.0	2.1	3.8	26
IRAS16065-5158	4.0	0.54	2.9	3.2	3.6	81
NGC6334I	1.7	0.24	2.6	15	3.7	70
IRAS17233-3606	1.0	0.13	0.3	5.0	6.2	44
SgrB2(N)[a]	7.8	1.05 – 0.69	8.4 – 11	2.4 – 7.4	84 – 119	10 – 7
SgrB2(M)[a]	7.8	1.23 – 0.69	63 – 50	13 – 34	220 – 167	29 – 42
G10.47+0.03	10.6	1.30	7.0	1.3	23	30
G31.41+0.31	7.9	1.02	2.6	0.8	12	22
G34.26+0.15	3.7	0.52	4.7	5.5	13	36
W51d	5.4	0.79	24	12	38	63
W51e	5.4	0.76	12	6.6	38	32

proto-SSC Source	D (Mpc)	R (pc)	L_{IR} (10^7 $L_\odot$)	Σ_{IR} (10^7 $L_\odot$ pc^{-2})	M_{H_2} (10^5 $M_\odot$)	L_{IR}/M_{H_2} ($L_\odot/M_\odot$)
proto-SSC 13	3.5	1.5	9.4	1.3	9.5	99

BGN Source	D (Mpc)	R (pc)	L_{IR} (10^{11} $L_\odot$)	Σ_{IR} (10^7 $L_\odot$ pc^{-2})	M_{H_2} (10^9 $M_\odot$)	L_{IR}/M_{H_2} ($L_\odot/M_\odot$)
NGC4418	34	11.7 – 13.5	0.9 – 1.3	22	0.3	273 – 394
Arp220W	85	47 – 60	7.6 – 12	11	5.5[b]	137 – 217
Arp220E	85	87 – 90	1.3 – 2.4	0.5 – 1.0	1.0[b]	127 – 234
Zw049.057	56	15 – 25	1.0 – 1.4	5.0 – 20	1.1	92 – 128
IC860	59	14.5 – 20	0.4 – 0.7	5.5	0.2	200 – 350
Mrk231	192	55 – 73	18 – 21	11 – 22	7.1	254 – 296

[a] In addition, the values from Etxaluze et al. (2013) are given for SgrB2(N) and SgrB2(M).
[b] Masses for Arp 220W and Arp 220E have been roughly estimated from the Arp 220 total mass (6.6×10^9 $M_\odot$) assuming each contributes in mass the same they do for the total luminosity.

with $T_{vib} \gtrsim 400$ K towards the center of proto-SSC 13a. From the velocity map we observe a velocity structure, with a large region with velocities of 250 – 263 km s^{-1} and a smaller region with velocities of 243 – 250 km s^{-1}. The derived LTE dust temperatures overestimate the actual dust temperatures due to opacity effects and dust temperature gradients in the SHC.

(3) We have also carried out, for the first time, a multi-transition non-local modelling of the spatial distribution of the HC_3N* line emission profiles including the ground state and vibrationally excited states $v_7 = 1$, $v_7 = 2$, $v_6 = 1$, $v_5/v_7 = 3$, $v_6 = v_7 = 1$, $v_4 = 1$, and $v_6 = 2$. The models are self-consistent with the continuum emission radial profile and take into account the greenhouse effect for different H_2 density profiles. Radial profiles of the observed HC_3N* line emission were produced by averaging the spectra in rings of 0.1 pc thickness up to a radius of 1.5 pc to increase the signal to noise ratio. Models only considering the continuum emission are very degenerated. The degeneration is broken when the radial profile of the HC_3N* emission is also considered. While the high-energy line emission can be explained either with high T_{dust} or moderate T_{dust} with high $N(HC_3N)$, this degeneracy is solved when including the low-energy lines in the analysis, indicating that $T_{dust} \lesssim 500$ K and $N(HC_3N) \sim 3\times10^{17}$ cm^{-2} reproduce essentially all the data. From the model that best fits the data we obtain a luminosity of $L_{IR} = 9.4\times10^7$ $L_\odot$, similar to the value obtained in Rico-Villas et al. (2020) and a mass of $M_{H_2} = 9.5\times10^5$ $M_\odot$, higher than that derived in Rico-Villas et al. (2020).

(4) The best-fit model assumes spatially distributed star formation proportional to the mass and density at each radii, with an H_2 density power law index of $q = 1.5$ ($q = 1$ in the outermost regions). In contrast, models with highly concentrated star formation only taking place at the center, despite reaching similar temperatures at the outer regions, they are unable to reproduce the high-v and low-v spatial profiles simultaneously. Therefore, the results from the best-fit model would be in accordance with the competitive accretion scenario, with the most massive stars located at the center and mass segregation is taking place at very early times.

(5) We have discussed the possible nature of the velocity change observed from the 2D LTE analysis perpendicular to the rotation plane of NGC 253. We conclude that cloud-cloud collision is the most likely explanation. Such a scenario would explain the velocity structure and the bridge feature observed in the $p-v$ diagrams. A rough analysis indicates that the collision between the two clouds provides the ram pressure required to trigger the star formation in proto-SSC 13a. This high pressure together with the shock resulting from the collision would be able to compress the gas and set the conditions for rapid massive star formation with high efficiencies.

(6) From the derived M_{H_2}, we find that proto-SSC 13a is in a super-criticial virial state with a virial parameter $\alpha \approx 0.21$, suggesting that

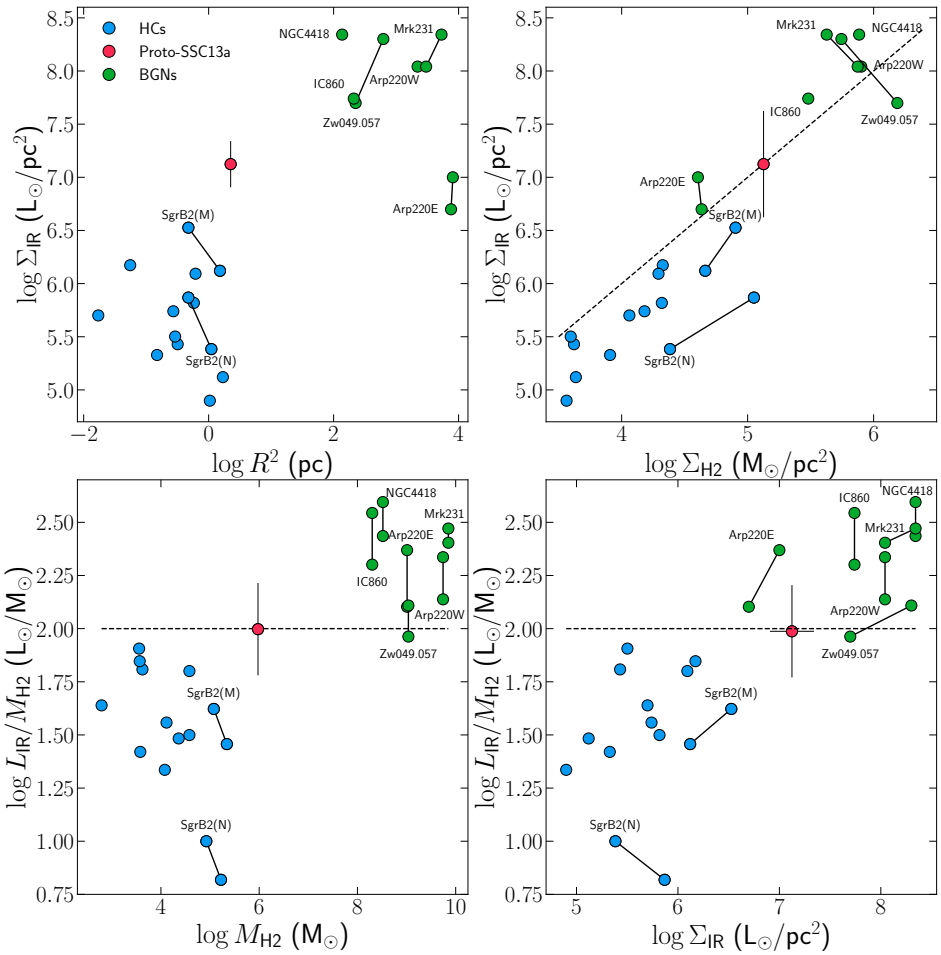

Figure 13. Comparison between the derived properties of proto-SSC 13a (red circle) to Milky Way HCs (blue circles) and BGNs from (U)LIRGs (green circles). Top left panel shows the luminosity surface density as a function of the squared source radius. Top right panel shows the luminosity surface density against the surface density. The dashed line indicates the relationship between Σ_{IR} and Σ_{H_2} for $L_{IR}/M_{H_2} = 100\,L_\odot\,M_\odot^{-1}$. Bottom left and bottom right panels show the luminosity per unit of gas mass as a function of the gas mass and the luminosity surface density, respectively. The error bars for proto-SSC 13a show the assumed error of 50% in luminosity due to varying X_d. Dashed lines indicate where $L_{IR}/M_{H_2} = 100\,L_\odot\,M_\odot^{-1}$.

proto-SSC 13a is going through a rapid collapse. We also find that L_{Edd} is an order of magnitude larger than the derived L_{IR}, meaning that radiation pressure is not able to halt the collapse.

(7) We infer a short free-fall time of $t_{ff} = 3 \times 10^4$ yr that, together with the derived small virial parameter, indicates that proto-SSC 13 is indeed very young. Proto-SSC 13a seems to be forming stars at SFR= $5\,M_\odot\,yr^{-1}$, which implies a short depletion time of $t_{dep} = 2 \times 10^5 \sim 6t_{ff}$.

(8) From the comparison of proto-SSC 13a with other deeply embedded star forming regions in the Milky Way HCs and the BGNs of (U)LIRGs, we observe a trend with higher luminosity surface density (Σ_{IR}) for higher molecular gas mass surface density (Σ_{H_2}). However, for the pure star-forming HCs and proto-SSC 13a, there seems to be an upper limit in L_{IR}/M_{H_2} of $100\,L_\odot\,M_\odot^{-1}$, similar to that found for non-interacting star forming galaxies. Since SSCs are among the most condensed and extreme star formation modes known, we argue that the excess in L_{IR}/M_{H_2} above $\sim 100\,L_\odot\,M_\odot^{-1}$ observed in BGNs most probably arises from the contribution of a buried AGN.

ACKNOWLEDGEMENTS

This paper makes use of ALMA data in projects 2018.1.01395.S (PI: Rico-Villas, Fernando) and 2017.1.00433.S (PI:Bolatto, Alberto). ALMA is a partnership of ESO (representing its member states), NSF (USA) and NINS (Japan), together with NRC (Canada) and NSC and ASIAA (Taiwan) and KASI (Republic of Korea), in cooperation with the Republic of Chile. The Joint ALMA Observatory is operated by ESO, AUI/NRAO and NAOJ.

F.R.V acknowledges financial support to the Spanish Ministry of Science and Innovation (MCIN) under grant number ESP2017-86582-C4-1-R, PID2019-105552RB-C41, and PhD fellowship BES-2016-078808, to the State Research Agency (AEI) with DOI 10.13039/501100011033 under project number PID2019-105552RB-C41 and to MDM-2017-0737 Unidad de Excelencia María de Maeztu.

V.M.R. is funded by the Agencia Estatal de Investigación (AEI) through the Ramón y Cajal programme (grant RYC2020-029387-I).

DATA AVAILABILITY

The data underlying this article were accessed from the ALMA Science Archive (`http://almascience.eso.org/asax/`), with the corresponding project identifiers listed on Table 3. The derived data generated in this research will be shared on reasonable request to the corresponding author.

REFERENCES

Anand G. S., et al., 2021, MNRAS, 501, 3621
Andrews B. H., Thompson T. A., 2011, ApJ, 727, 97
Beck S., 2015, International Journal of Modern Physics D, 24, 1530002
Bonnell I. A., Bate M. R., Clarke C. J., Pringle J. E., 1997, MNRAS, 285, 201
Bonnell I. A., Bate M. R., Clarke C. J., Pringle J. E., 2001, MNRAS, 323, 785
Bonnell I. A., Larson R. B., Zinnecker H., 2007, in Reipurth B., Jewitt D., Keil K., eds, Protostars and Planets V. p. 149 (arXiv:astro-ph/0603447)
Bressert E., Ginsburg A., Bally J., Battersby C., Longmore S., Testi L., 2012, ApJ, 758, L28
Cortes P. C., et al., 2022, ALMA Cycle 9 Technical Handbook. https://almascience.eso.org/documents-and-tools/cycle9/alma-technical-handbook
Costagliola F., Aalto S., 2010, A&A, 515, A71
Donnison J. R., Williams I. P., 1976, Nature, 261, 674
Elmegreen B. G., Efremov Y. N., 1997, ApJ, 480, 235
Etxaluze M., et al., 2013, A&A, 556, A137
Falstad N., et al., 2021, A&A, 649, A105
Finn M. K., Johnson K. E., Brogan C. L., Wilson C. D., Indebetouw R., Harris W. E., Kamenetzky J., Bemis A., 2019, ApJ, 874, 120
Fujita S., et al., 2021, PASJ, 73, S172
Fukui Y., et al., 2016, ApJ, 820, 26
Fukui Y., et al., 2018, ApJ, 859, 166
Furukawa N., Dawson J. R., Ohama A., Kawamura A., Mizuno N., Onishi T., Fukui Y., 2009, ApJ, 696, L115
Gao Y., Solomon P. M., 2004, ApJ, 606, 271
Gelatt A. E., Hunter D. A., Gallagher J. S., 2001, PASP, 113, 142
González-Alfonso E., Cernicharo J., 1997, A&A, 322, 938
González-Alfonso E., Cernicharo J., 1999, ApJ, 525, 845
González-Alfonso E., Sakamoto K., 2019, ApJ, 882, 153
González-Alfonso E., et al., 2015, ApJ, 800, 69
Graciá-Carpio J., et al., 2011, ApJ, 728, L7
Habe A., Ohta K., 1992, PASJ, 44, 203
Haghi H., Hoseini-Rad S. M., Zonoozi A. H., Küpper A. H. W., 2014, MNRAS, 444, 3699
Haworth T. J., Shima K., Tasker E. J., Fukui Y., Torii K., Dale J. E., Takahira K., Habe A., 2015, MNRAS, 454, 1634
Ho L. C., Filippenko A. V., 1996a, ApJ, 466, L83
Ho L. C., Filippenko A. V., 1996b, ApJ, 472, 600
Inoue T., Fukui Y., 2013, ApJ, 774, L31
Ivezic Z., Elitzur M., 1997, MNRAS, 287, 799
Johnson K. E., Leroy A. K., Indebetouw R., Brogan C. L., Whitmore B. C., Hibbard J., Sheth K., Evans A. S., 2015, ApJ, 806, 35
Karachentsev I. D., Tully R. B., Anand G. S., Rizzi L., Shaya E. J., 2021, AJ, 161, 205
Kauffmann J., Pillai T., Goldsmith P. F., 2013, ApJ, 779, 185
Kennicutt Robert C. J., 1998, ARA&A, 36, 189
Kepley A. A., Tsutsumi T., Brogan C. L., Indebetouw R., Yoon I., Mason B., Donovan Meyer J., 2020, PASP, 132, 024505
Krieger N., et al., 2019, ApJ, 881, 43
Krumholz M. R., et al., 2014, in Beuther H., Klessen R. S., Dullemond C. P., Henning T., eds, Protostars and Planets VI. p. 243 (arXiv:1401.2473), doi:10.2458/azu_uapress_9780816531240-ch011
Leroy A. K., et al., 2018, ApJ, 869, 126
Levy R. C., et al., 2021, ApJ, 912, 4
Martín S., Martín-Pintado J., Blanco-Sánchez C., Rivilla V. M., Rodríguez-Franco A., Rico-Villas F., 2019, A&A, 631, A159
McCrady N., Graham J. R., Vacca W. D., 2005, ApJ, 621, 278
McMillan S. L. W., Vesperini E., Portegies Zwart S. F., 2007, ApJ, 655, L45
McMullin J. P., Waters B., Schiebel D., Young W., Golap K., 2007, in Shaw R. A., Hill F., Bell D. J., eds, Astronomical Society of the Pacific Conference Series Vol. 376, Astronomical Data Analysis Software and Systems XVI. p. 127
Melnick J., Moles M., Terlevich R., 1985, A&A, 149, L24
Melo V. P., Muñoz-Tuñón C., Maíz-Apellániz J., Tenorio-Tagle G., 2005, ApJ, 619, 270
Mengel S., Lehnert M. D., Thatte N. A., Vacca W. D., Whitmore B., Chandar R., 2008, A&A, 489, 1091
Meurer G. R., Heckman T. M., Leitherer C., Kinney A., Robert C., Garnett D. R., 1995, AJ, 110, 2665
Mills E. A. C., et al., 2021, arXiv e-prints, p. arXiv:2106.14970
Müller H. S. P., Thorwirth S., Roth D. A., Winnewisser G., 2001, A&A, 370, L49
Müller H. S. P., Schlöder F., Stutzki J., Winnewisser G., 2005, Journal of Molecular Structure, 742, 215
Murray N., Chang P., 2012, ApJ, 746, 75
Murray N., Quataert E., Thompson T. A., 2005, ApJ, 618, 569
O'Connell R. W., Gallagher John S. I., Hunter D. A., 1994, ApJ, 433, 65
Ohama A., et al., 2010, ApJ, 709, 975
Pavlík V., Kroupa P., Šubr L., 2019, A&A, 626, A79
Portegies Zwart S. F., McMillan S. L. W., Gieles M., 2010, ARA&A, 48, 431
Rekola R., Richer M. G., McCall M. L., Valtonen M. J., Kotilainen J. K., Flynn C., 2005, MNRAS, 361, 330
Rico-Villas F., Martín-Pintado J., González-Alfonso E., Martín S., Rivilla V. M., 2020, MNRAS, 491, 4573
Rico-Villas F., Martín-Pintado J., González-Alfonso E., Rivilla V. M., Martín S., García-Burillo S., Jiménez-Serra I., Sánchez-García M., 2021, MNRAS, 502, 3021
Rolffs R., Schilke P., Wyrowski F., Menten K. M., Güsten R., Bisschop S. E., 2011, A&A, 527, A68
Rowan-Robinson M., 1982, Models for hot-centred galactic clouds. pp 47–68
Skinner M. A., Ostriker E. C., 2015, ApJ, 809, 187
Solomon P. M., Sage L. J., 1988, ApJ, 334, 613
Takahira K., Tasker E. J., Habe A., 2014, ApJ, 792, 63
Tremonti C. A., Calzetti D., Leitherer C., Heckman T. M., 2001, ApJ, 555, 322
Tsuge K., Tachihara K., Fukui Y., Sano H., Tokuda K., Ueda J., Iono D., 2021, PASJ, 73, 417
Turner J. L., Beck S. C., 2004, ApJ, 602, L85
Ulvestad J. S., Antonucci R. R. J., 1997, ApJ, 488, 621
Vanzi L., 2003, A&A, 408, 523
Watson A. M., et al., 1996, AJ, 112, 534
Whitmore B. C., Schweizer F., 1995, AJ, 109, 960
Whitmore B. C., Schweizer F., Leitherer C., Borne K., Robert C., 1993, AJ, 106, 1354
Whitmore B. C., Zhang Q., Leitherer C., Fall S. M., Schweizer F., Miller B. W., 1999, AJ, 118, 1551

APPENDIX A: PROTO-SSC 13A AVERAGED RING SPECTRA AND SLIM LTE MODEL FIGURES

To increase the signal-to-noise ratio of our data, we have averaged the spectra within rings of 0.1 pc thickness from the center of proto-SSC 13a (i.e. $r = 0$) up to a radius of 1.5 pc, increasing the signal-to-noise ratio for the higher energy HC_3N^* transitions. We consider the center of the rings to be the position of the brightest continuum emission at 219 GHz, i.e. RA(J2000)= $00^h47^m33^s.1970$; Dec(J2000)= $-25°17'16''.733$.

The following figures show the averaged spectra (black histogram lines) inside these rings towards proto-SSC 13a. Overlaid is also the modelled `SLIM` LTE emission from the HC_3N^* $J = 24-23$ transitions (in green) and from the HC_3N^* $J = 26 - 25$ transitions. The sum of the `SLIM` fitted LTE profiles for all species is shown with dashed red lines. With the fitted parameters, `SLIM` models the emission of all the HC_3N^* transitions even if not considered for the fit. Therefore, some undetected lines from high vibrational states show modelled emission within noise level. The inner and outer radii of the rings, the number of pixels and the derived properties from the modelling are listed in Table 6. The figures show the HC_3N^* transitions vibrational state in black, with the quantum numbers of the upper level of the transition in parenthesis, i.e. (l_{up}) or (l_{up}, k_{up}). Labels for transitions from other species are indicated in grey.

APPENDIX B: OBSERVED TRANSITIONS

Table B1 lists the HC_3N^* transitions vibrational state and quantum numbers in the observed frequency range.

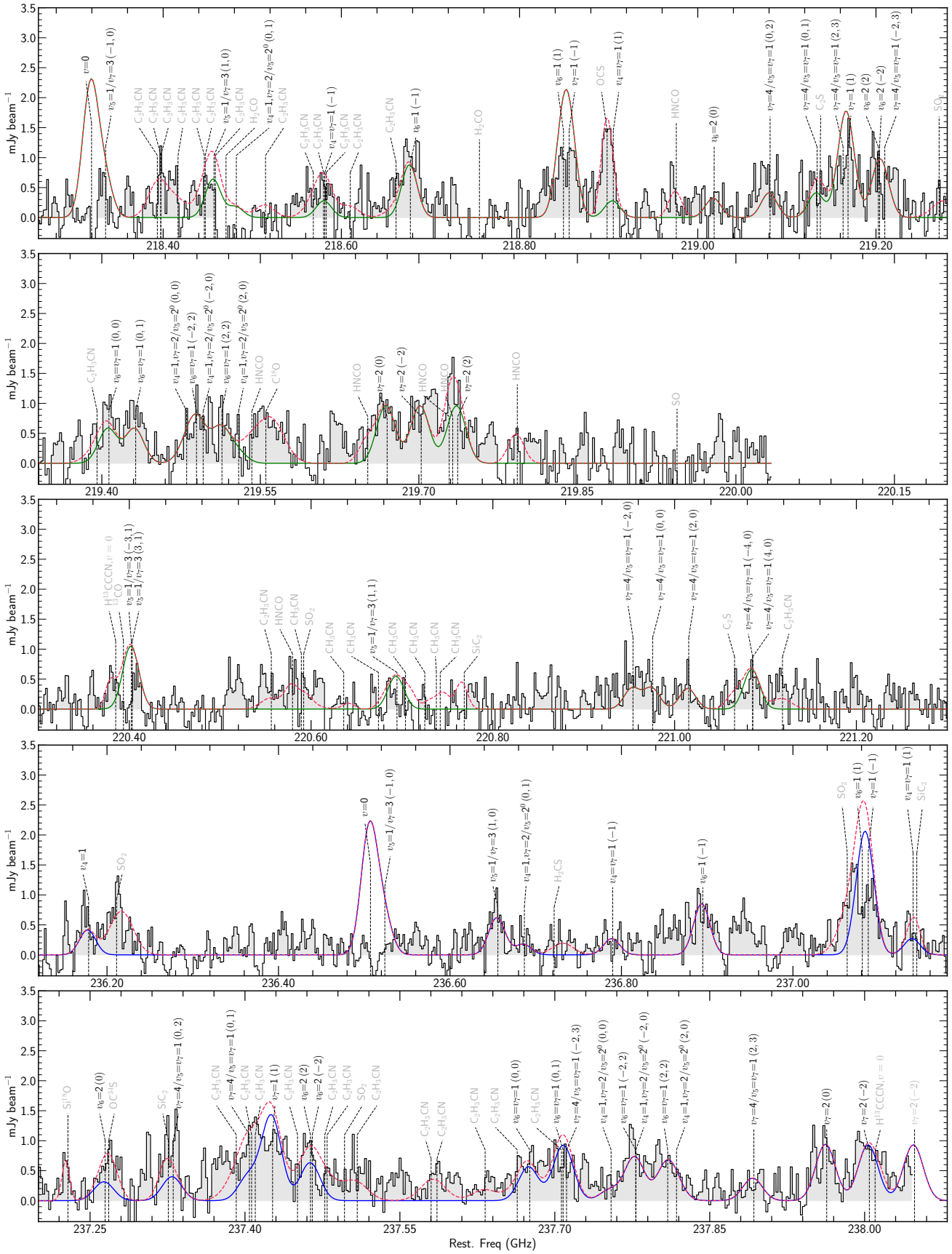

Figure A1. Proto-SSC 13a HC_3N* averaged spectra and SLIM LTE emission (red line) for the different averaged ring emission from the ring enclosing the pixels with distances between 0.0 pc and 0.1 pc.

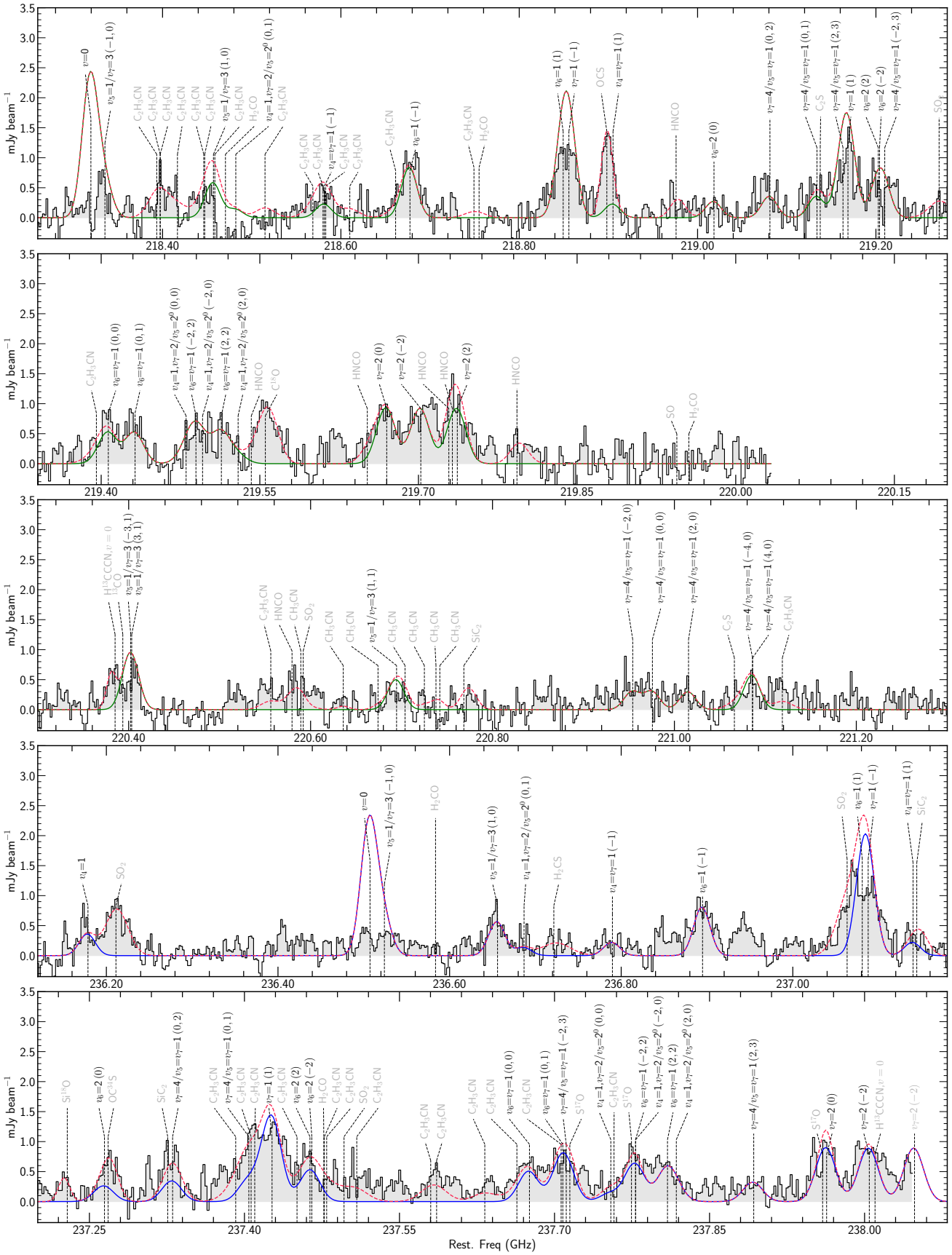

Figure A2. Proto-SSC 13a HC_3N* averaged spectra and SLIM LTE emission (red line) for the different averaged ring emission from the ring enclosing the pixels with distances between 0.1 pc and 0.2 pc.

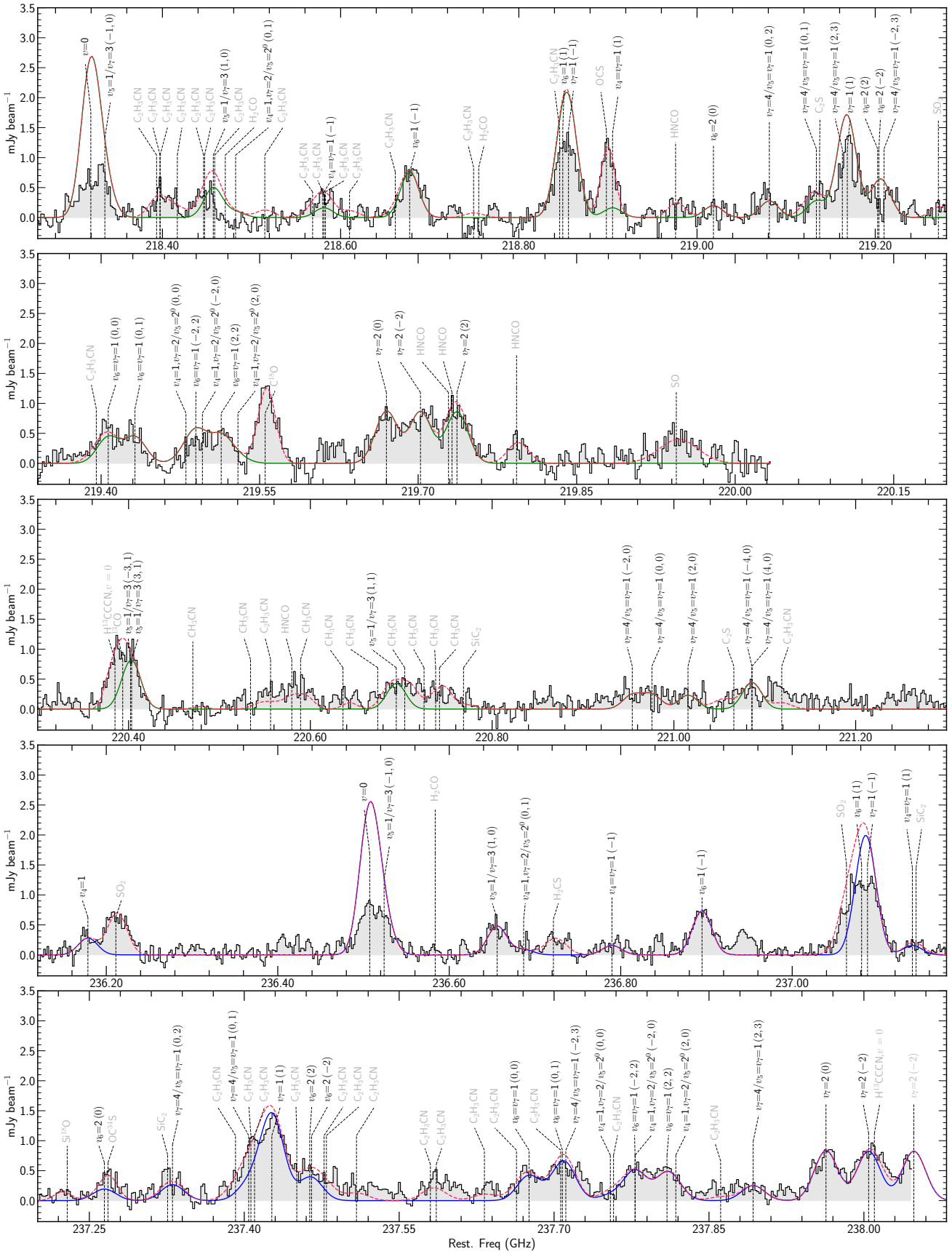

Figure A3. Proto-SSC 13a HC_3N* averaged spectra and SLIM LTE emission (red line) for the different averaged ring emission from the ring enclosing the pixels with distances between 0.2 pc and 0.3 pc.

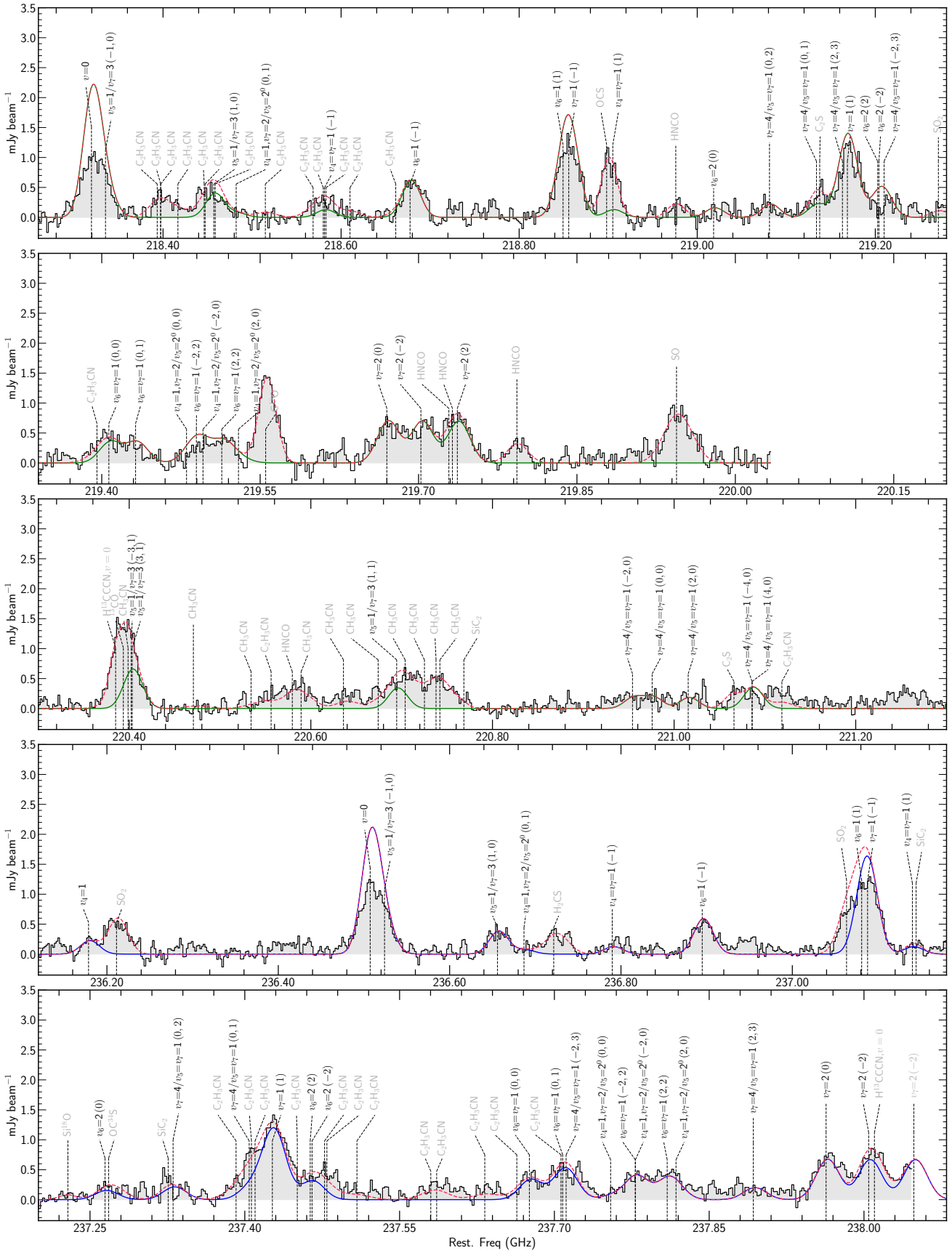

Figure A4. Proto-SSC 13a HC_3N* averaged spectra and SLIM LTE emission (red line) for the different averaged ring emission from the ring enclosing the pixels with distances between 0.3 pc and 0.4 pc.

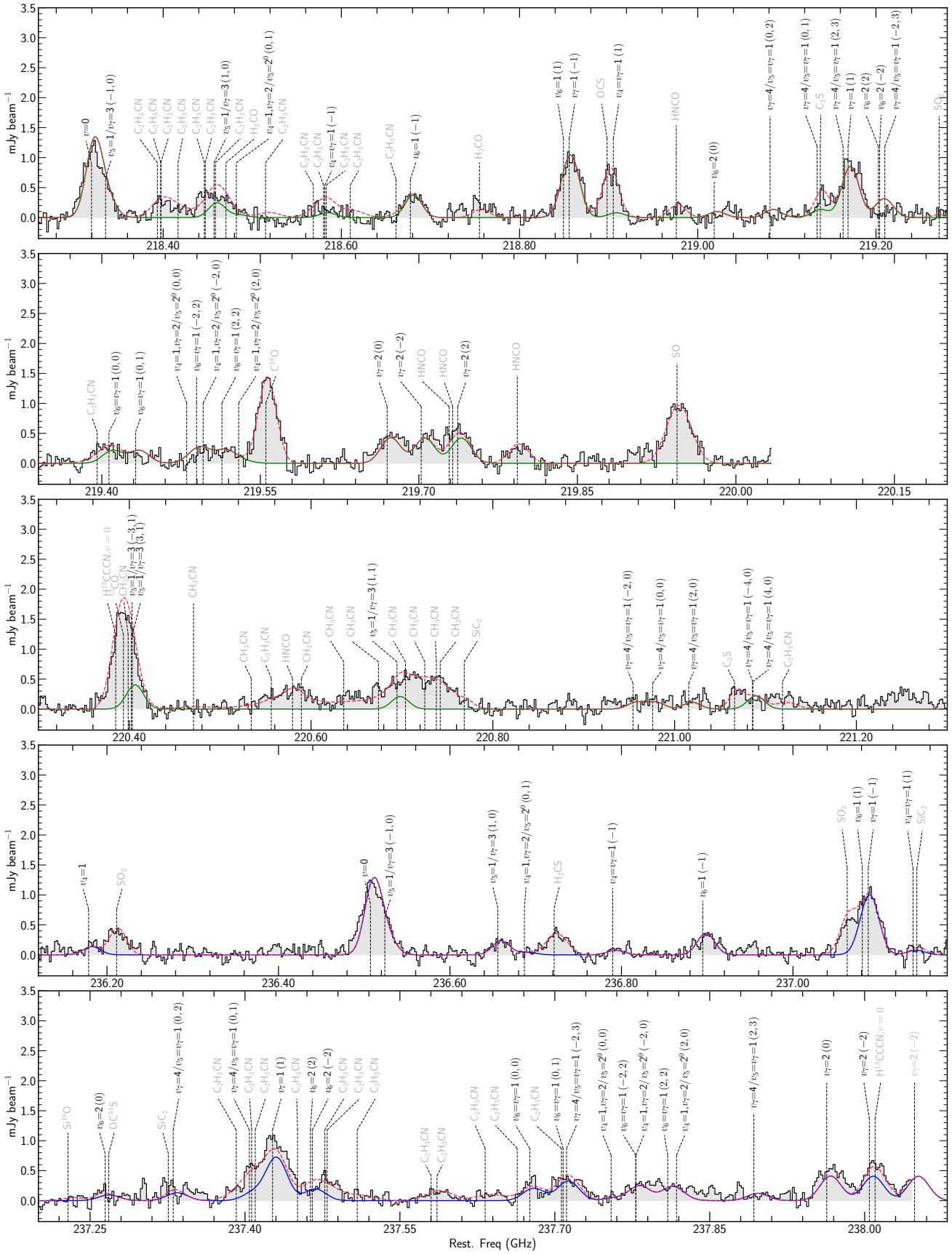

Figure A5. Proto-SSC 13a HC_3N* averaged spectra and SLIM LTE emission (red line) for the different averaged ring emission from the ring enclosing the pixels with distances between 0.4 pc and 0.5 pc.

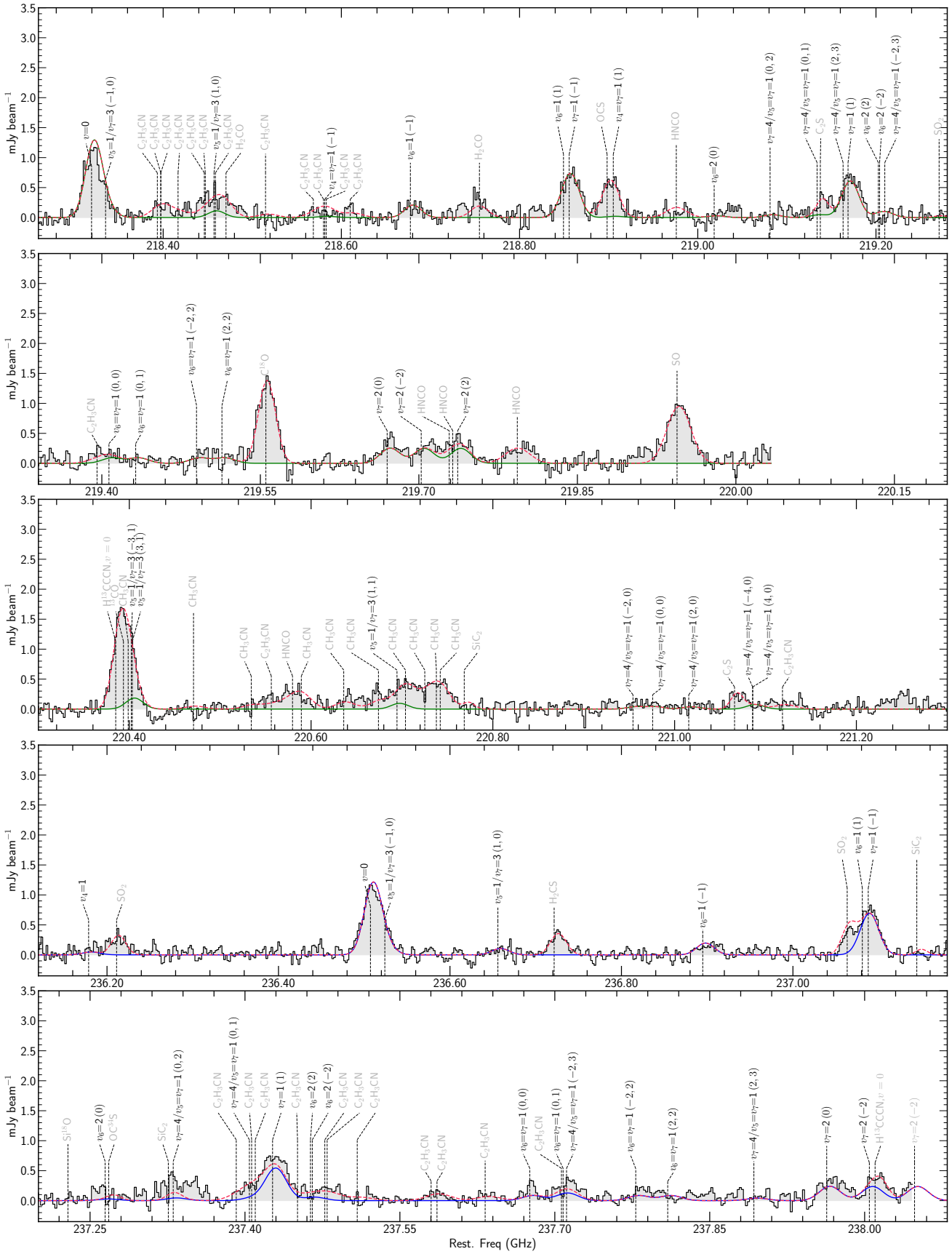

Figure A6. Proto-SSC 13a HC_3N* averaged spectra and SLIM LTE emission (red line) for the different averaged ring emission from the ring enclosing the pixels with distances between 0.5 pc and 0.6 pc.

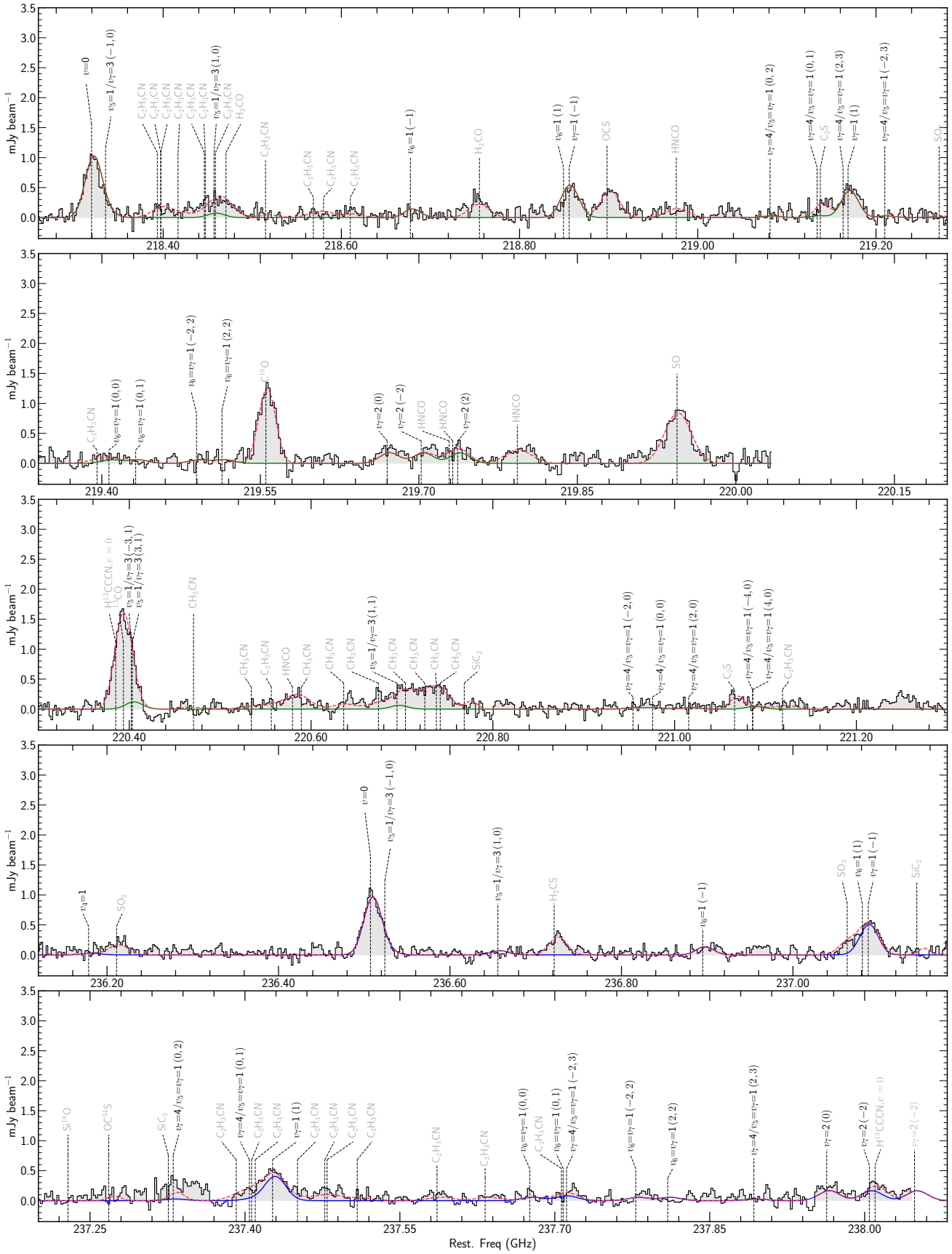

Figure A7. Proto-SSC 13a HC_3N* averaged spectra and SLIM LTE emission (red line) for the different averaged ring emission from the ring enclosing the pixels with distances between 0.6 pc and 0.7 pc.

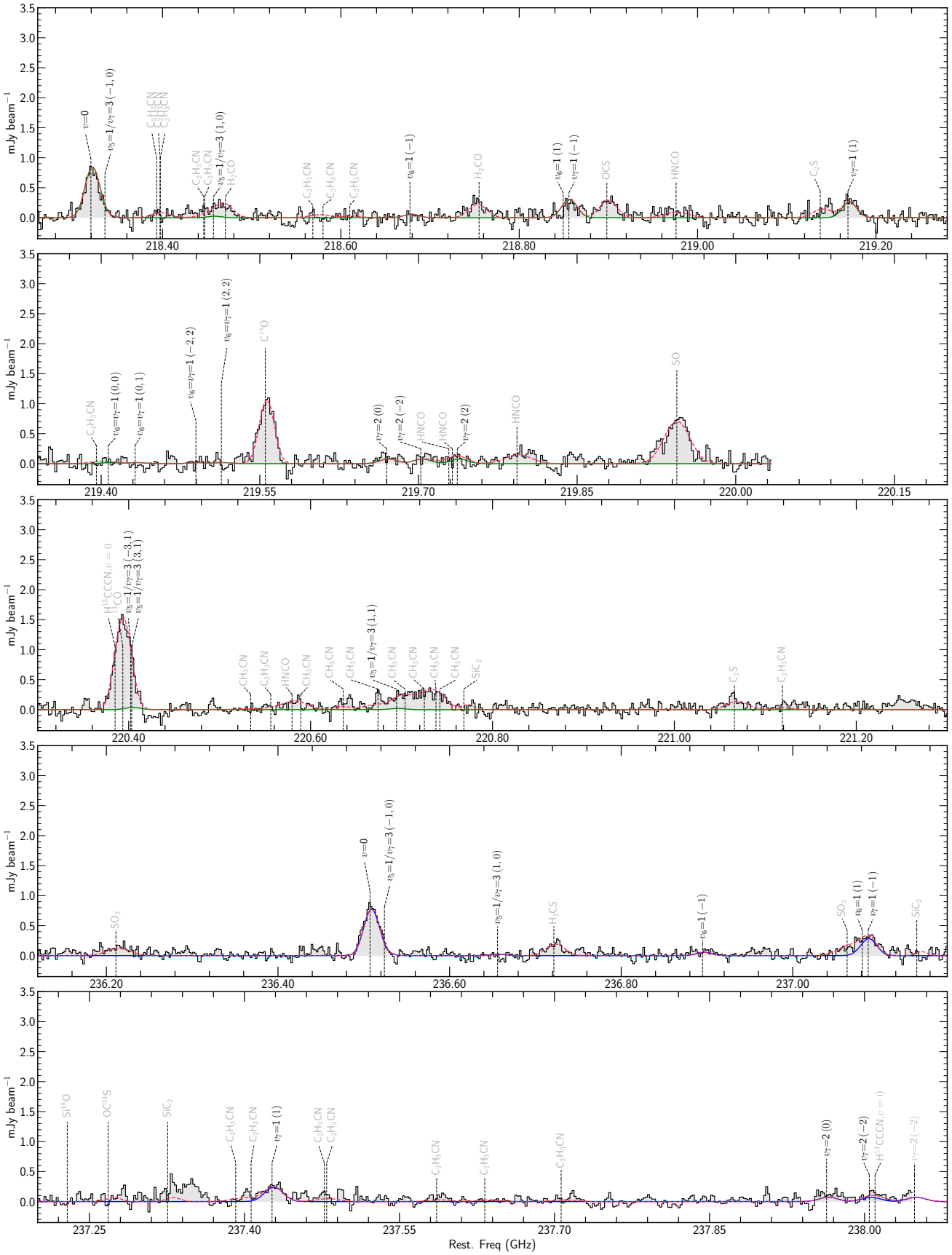

Figure A8. Proto-SSC 13a HC_3N* averaged spectra and SLIM LTE emission (red line) for the different averaged ring emission from the ring enclosing the pixels with distances between 0.7 pc and 0.8 pc.

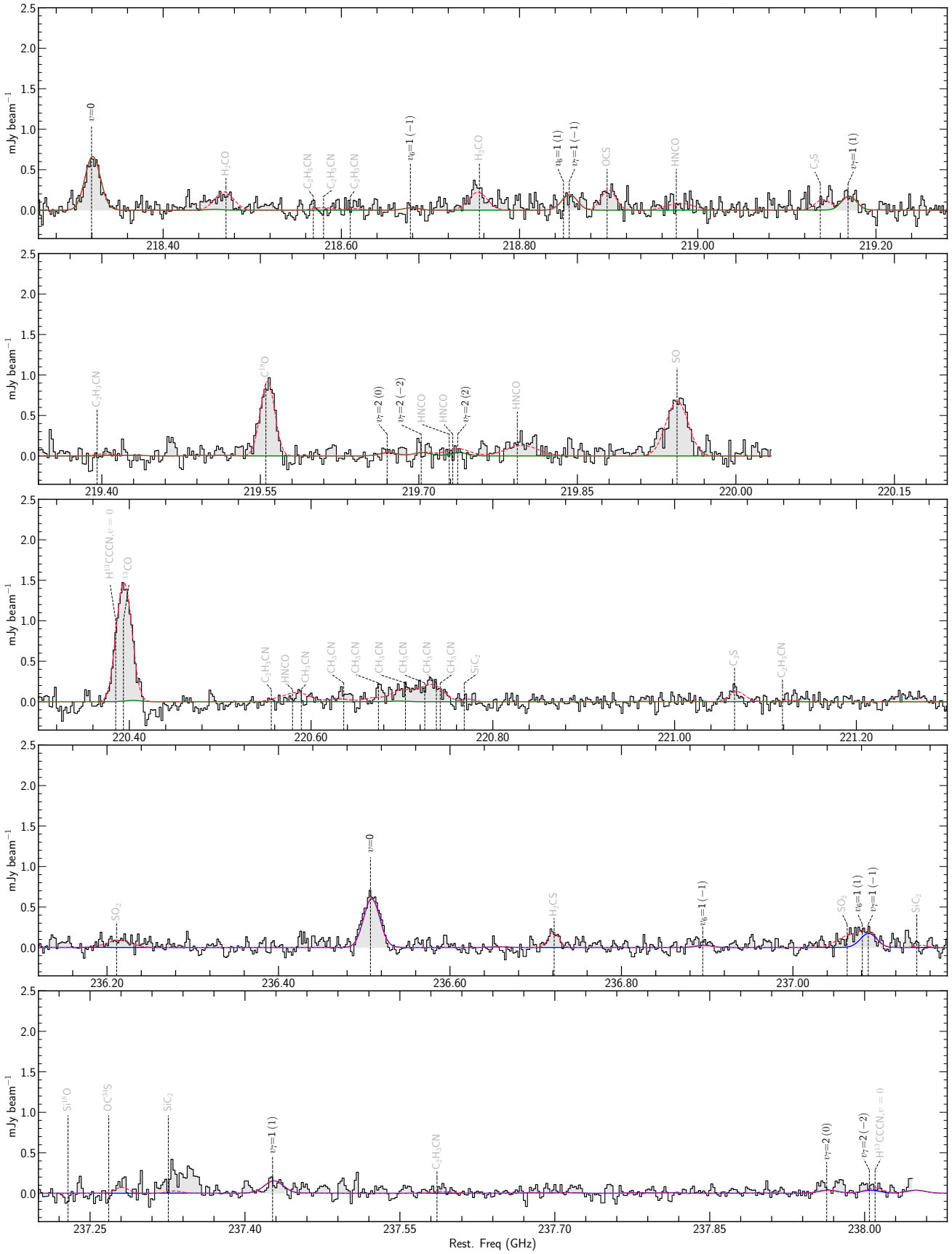

Figure A9. Proto-SSC 13a HC_3N* averaged spectra and SLIM LTE emission (red line) for the different averaged ring emission from the ring enclosing the pixels with distances between 0.8 pc and 0.9 pc.

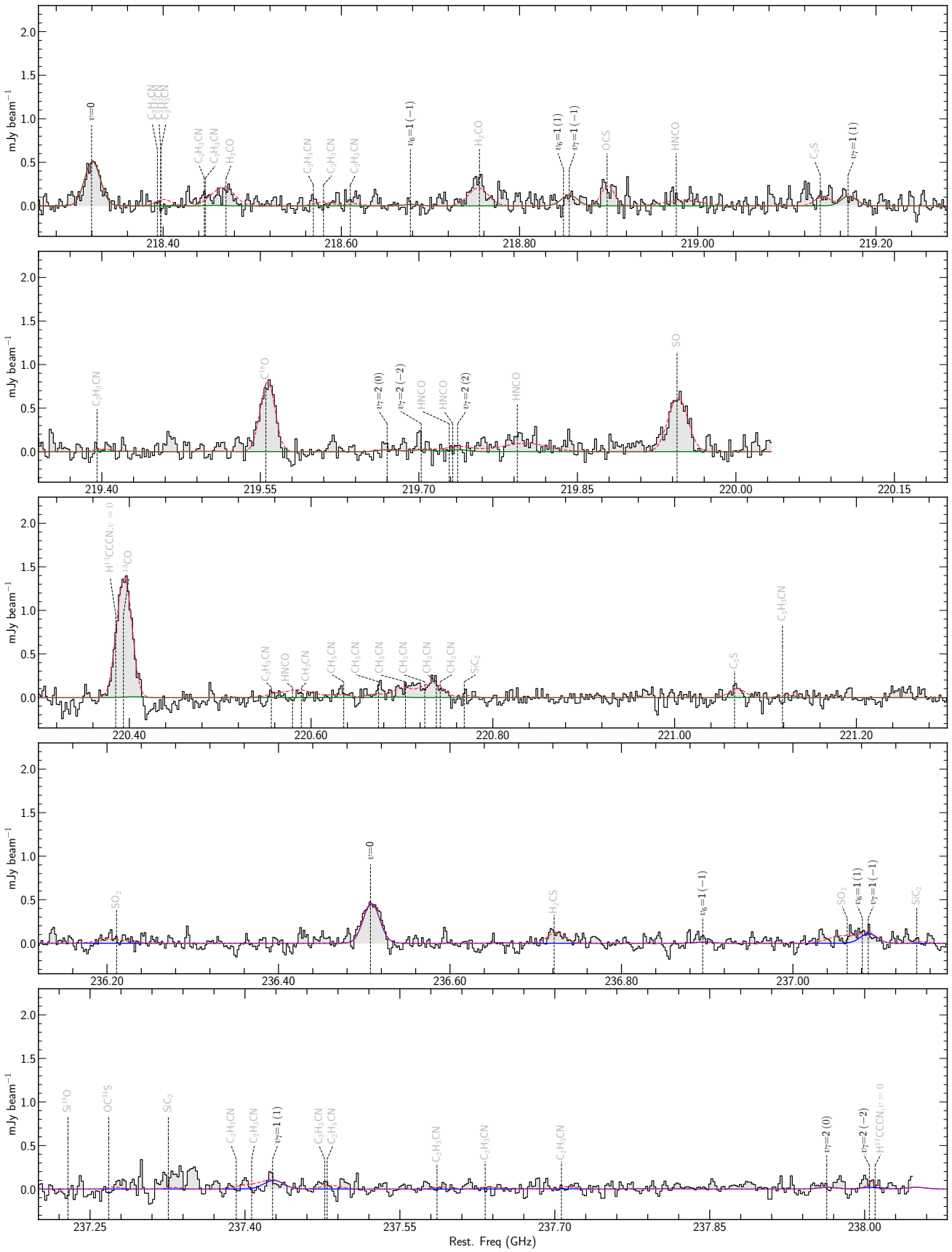

Figure A10. Proto-SSC 13a HC_3N* averaged spectra and `SLIM` LTE emission (red line) for the different averaged ring emission from the ring enclosing the pixels with distances between 0.9 pc and 1.0 pc.

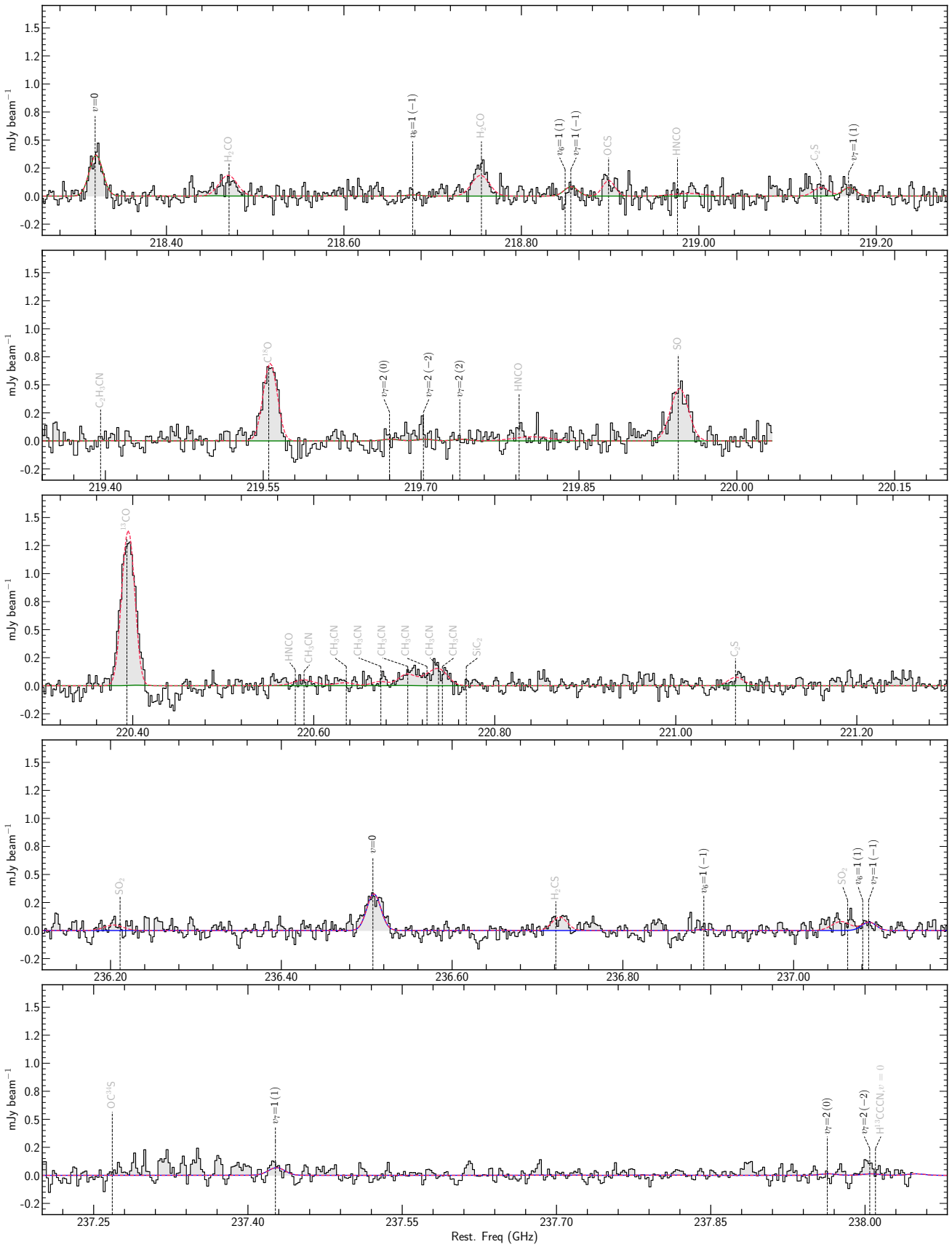

Figure A11. Proto-SSC 13a HC_3N* averaged spectra and `SLIM` LTE emission (red line) for the different averaged ring emission from the ring enclosing the pixels with distances between 1.0 pc and 1.1 pc.

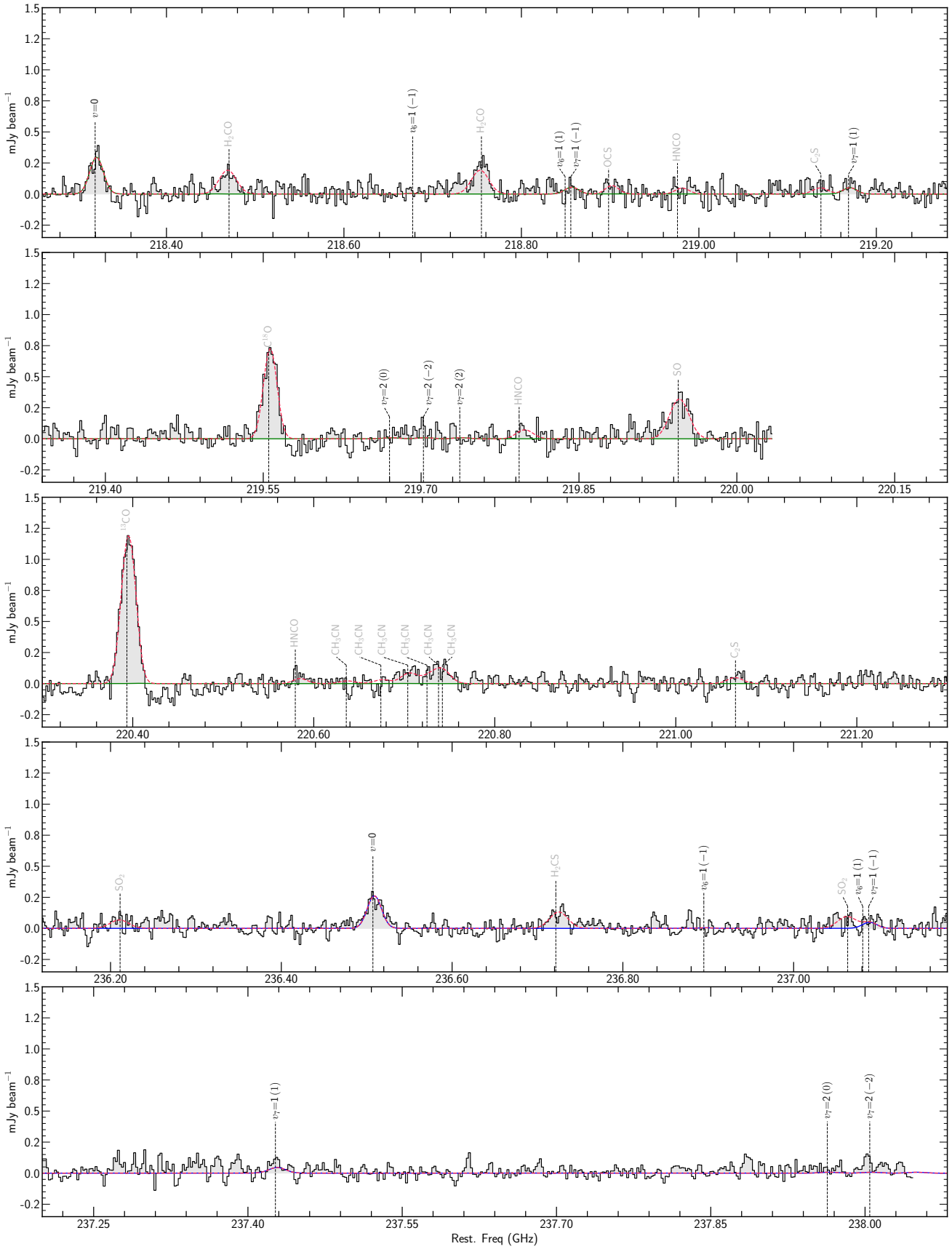

Figure A12. Proto-SSC 13a HC_3N* averaged spectra and `SLIM` LTE emission (red line) for the different averaged ring emission from the ring enclosing the pixels with distances between 1.1 pc and 1.2 pc.

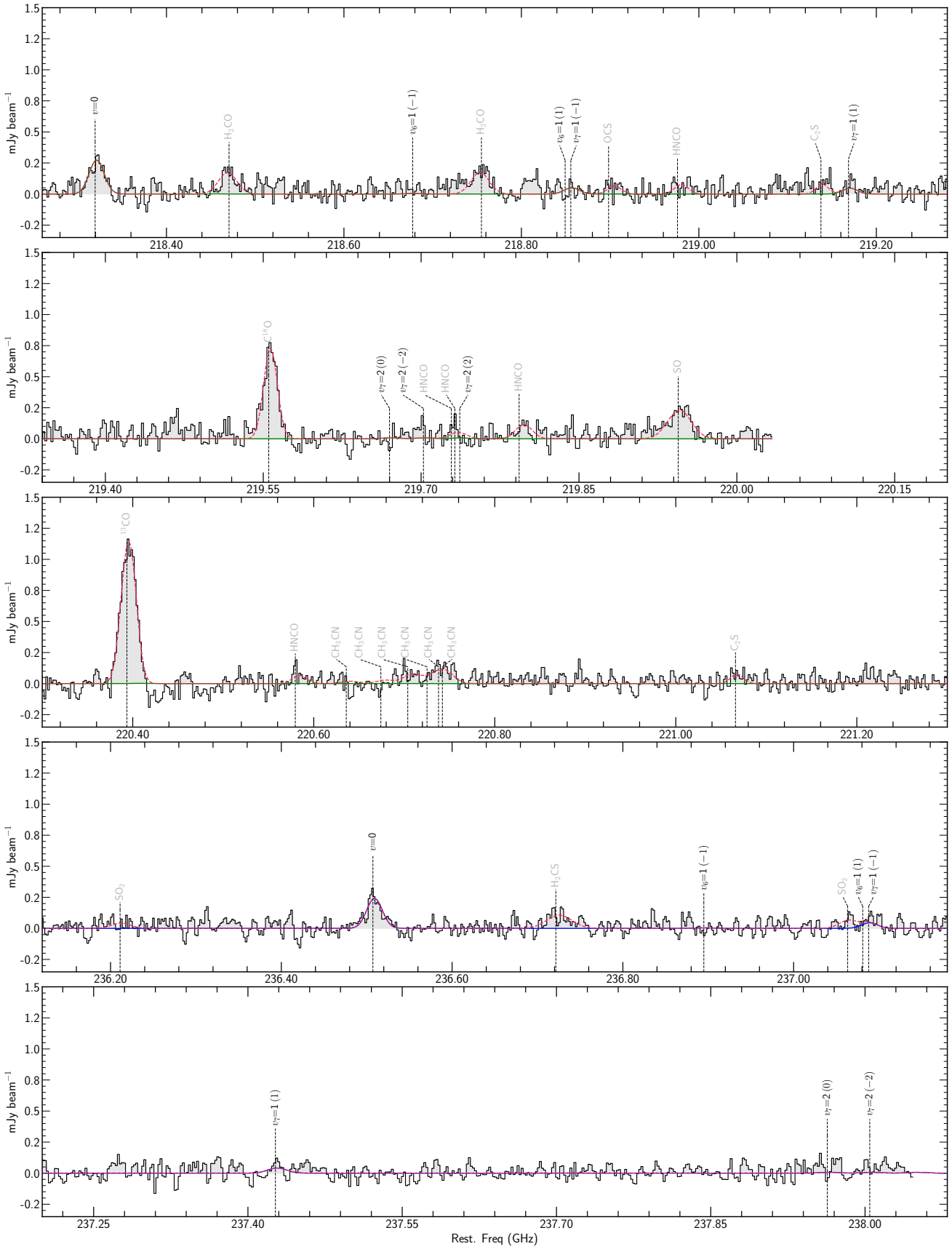

Figure A13. Proto-SSC 13a HC_3N* averaged spectra and `SLIM` LTE emission (red line) for the different averaged ring emission from the ring enclosing the pixels with distances between 1.2 pc and 1.3 pc.

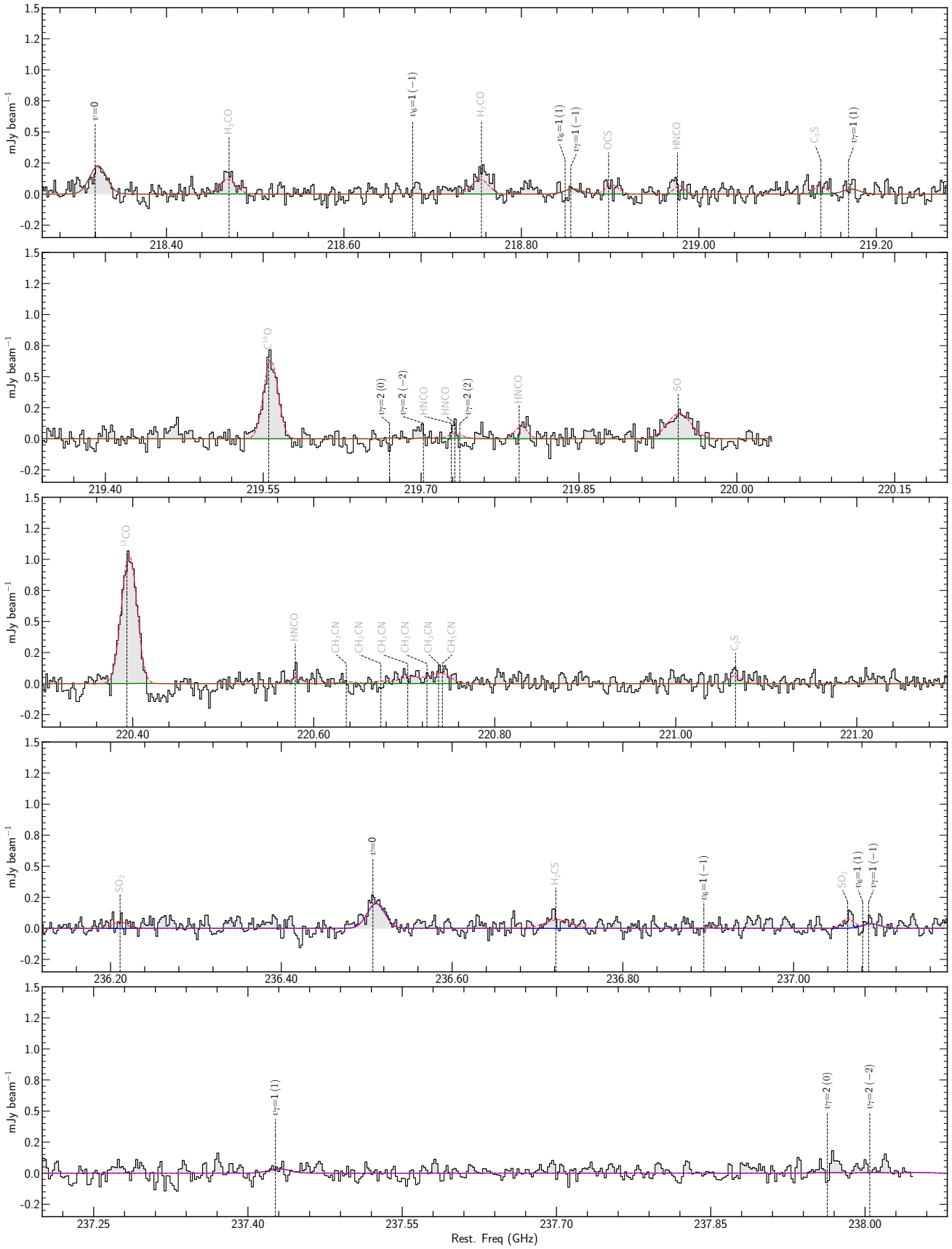

Figure A14. Proto-SSC 13a HC_3N* averaged spectra and `SLIM` LTE emission (red line) for the different averaged ring emission from the ring enclosing the pixels with distances between 1.3 pc and 1.4 pc.

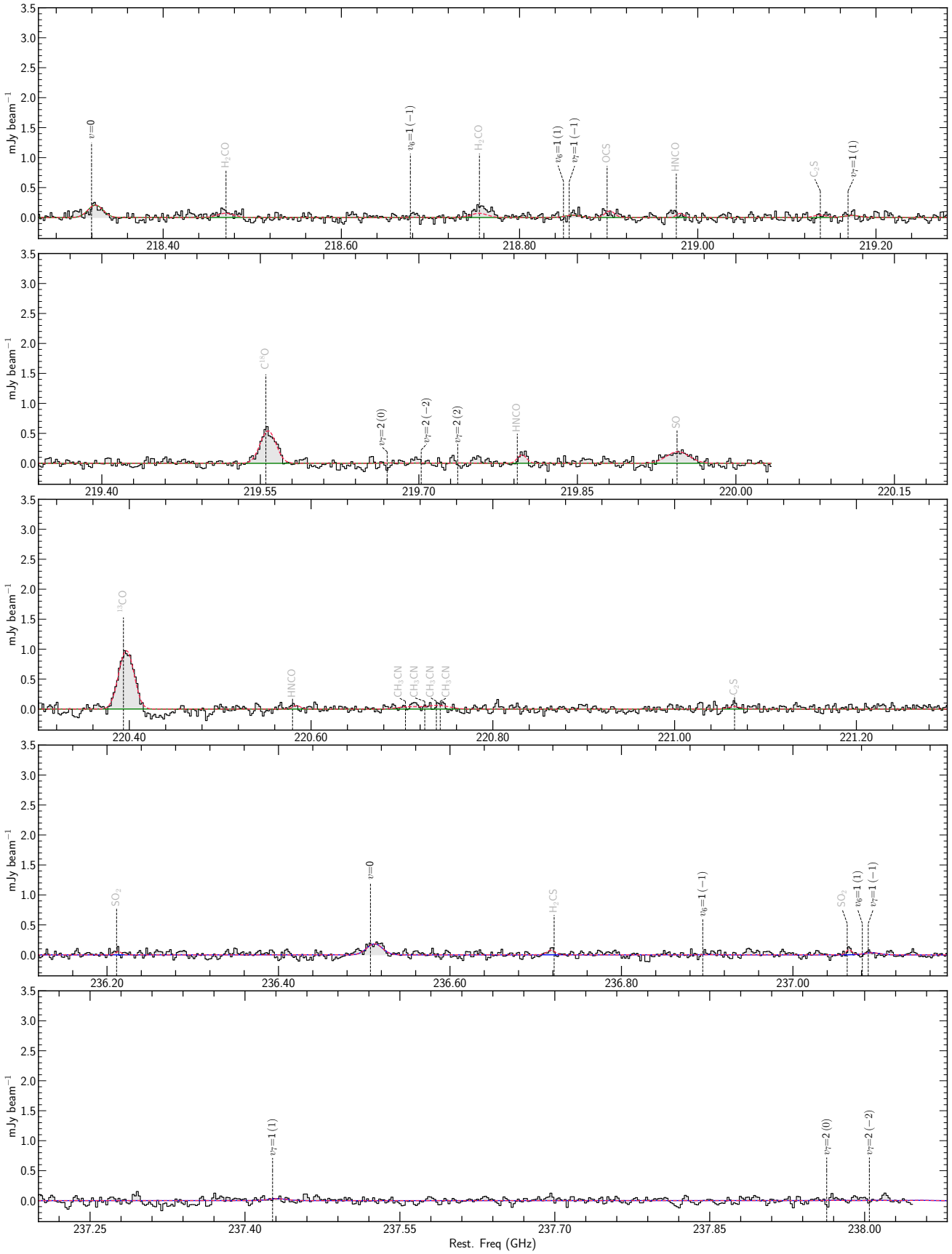

Figure A15. Proto-SSC 13a HC_3N* averaged spectra and SLIM LTE emission (red line) for the different averaged ring emission from the ring enclosing the pixels with distances between 1.4 pc and 1.5 pc.

Table B1: HC_3N* transitions vibrational state and quantum numbers in the observed frequency range. Also indicated is the energy of the upper state (E_{up}), the frequency, the logarithm of the Eintein-A_{ul} coefficients, the line strength logarithm at 300 K (log Int.) and if the line is detected (Det.) and contaminated (Cont.). When a line is both detected and contaminated it means that it is blended with another HC_3N transition or that it is slightly blended with another species.

Vib. State	J_{up}	l_{up}	k_{up}	J_{lo}	l_{lo}	k_{lo}	g_{up}	E_{up} (K)	ν (GHz)	log A_{ul} (s^{-1})	log Int. (nm^2 MHz)	Det.	Cont.
$v = 0$	24			23			49	131	218.32	-3.029	-1.295	Y	N
$v = 0$	26			25			53	153	236.51	-2.978	-1.222	Y	N
$v_7 = 1$	24	-1		23	1		49	452	218.86	-3.083	-1.760	Y	Y
$v_7 = 1$	24	1		23	-1		49	452	219.17	-3.081	-1.759	Y	N
$v_7 = 1$	26	-1		25	1		53	474	237.09	-2.978	-1.688	Y	Y
$v_7 = 1$	26	1		25	-1		53	475	237.43	-2.976	-1.687	Y	N
$v_7 = 2$	24	0		23	0		49	774	219.68	-3.079	-2.224	Y	N
$v_7 = 2$	24	-2		23	2		49	777	219.71	-3.082	-2.231	Y	Y
$v_7 = 2$	24	2		23	-2		49	777	219.74	-3.082	-2.231	Y	N
$v_7 = 2$	26	0		25	0		53	796	237.97	-2.974	-2.151	Y	N
$v_6 = 1$	24	-1		23	1		49	849	218.68	-2.976	-2.335	Y	N
$v_6 = 1$	24	1		23	-1		49	849	218.85	-3.082	-2.334	Y	Y
$v_6 = 1$	26	-1		25	1		53	871	236.9	-2.978	-2.262	Y	N
$v_6 = 1$	26	1		25	-1		53	871	237.09	-2.977	-2.261	Y	Y
$v_5 = 1/v_7 = 3$	24	-1	0	23	1	0	49	1085	218.34	-3.090	-2.683	Y	Y
$v_5 = 1/v_7 = 3$	24	1	0	23	-1	0	49	1085	218.46	-3.089	-2.682	Y	Y
$v_5 = 1/v_7 = 3$	24	1	1	23	-1	1	49	1087	220.7	-3.076	-2.679	Y	Y
$v_5 = 1/v_7 = 3$	24	-3	1	23	3	1	49	1094	220.41	-3.084	-2.677	Y	Y
$v_5 = 1/v_7 = 3$	24	3	1	23	-3	1	49	1094	220.41	-3.084	-2.693	Y	Y
$v_5 = 1/v_7 = 3$	26	-1	0	25	1	0	53	1107	236.53	-2.985	-2.693	Y	Y
$v_5 = 1/v_7 = 3$	26	1	0	25	-1	0	53	1107	236.66	-2.984	-2.610	Y	N
$v_6 = v_7 = 1$	24	0	0	23	0	0	49	1168	219.41	-3.080	-2.610	Y	Y
$v_6 = v_7 = 1$	24	0	1	23	0	1	49	1169	219.44	-3.080	-2.795	Y	N
$v_6 = v_7 = 1$	24	-2	2	23	2	2	49	1169	219.49	-3.082	-2.797	Y	N
$v_6 = v_7 = 1$	24	2	2	23	-2	2	49	1169	219.52	-3.082	-2.800	Y	N
$v_6 = v_7 = 1$	26	0	0	25	0	0	53	1190	237.68	-2.975	-2.800	Y	Y
$v_6 = v_7 = 1$	26	0	1	25	0	1	53	1192	237.71	-2.975	-2.723	Y	Y
$v_6 = v_7 = 1$	26	-2	2	25	2	2	53	1192	237.78	-2.977	-2.724	Y	N
$v_6 = v_7 = 1$	26	2	2	25	-2	2	53	1192	237.81	-2.977	-2.727	Y	N
$v_4 = 1$	26			25			53	1399	236.18	-2.996	-3.042	Y	N
$v_7 = 4/v_5 = v_7 = 1$	24	0	0	23	0	0	49	1404	220.98	-3.091	-3.150	N	N
$v_7 = 4/v_5 = v_7 = 1$	24	0	2	23	0	2	49	1406	219.09	-3.096	-3.155	Y	N
$v_7 = 4/v_5 = v_7 = 1$	24	-2	0	23	2	0	49	1407	220.96	-3.095	-3.159	N	N
$v_7 = 4/v_5 = v_7 = 1$	24	2	0	23	-2	0	49	1407	221.02	-3.095	-3.160	N	N
$v_7 = 4/v_5 = v_7 = 1$	24	2	3	23	-2	3	49	1407	219.17	-3.102	-3.162	Y	Y
$v_7 = 4/v_5 = v_7 = 1$	24	-2	3	23	2	3	49	1407	219.22	-3.100	-3.161	Y	Y
$v_7 = 4/v_5 = v_7 = 1$	24	0	1	23	0	1	49	1408	219.14	-3.096	-3.158	Y	Y
$v_7 = 4/v_5 = v_7 = 1$	24	-4	0	23	4	0	49	1416	221.09	-3.103	-3.180	Y	Y
$v_7 = 4/v_5 = v_7 = 1$	24	4	0	23	-4	0	49	1416	221.09	-3.103	-3.180	Y	Y
$v_7 = 4/v_5 = v_7 = 1$	26	0	2	25	0	2	53	1428	237.34	-2.992	-3.083	N	Y
$v_7 = 4/v_5 = v_7 = 1$	26	2	3	25	-2	3	53	1429	237.9	-3.017	-3.111	N	Y
$v_7 = 4/v_5 = v_7 = 1$	26	-2	3	25	2	3	53	1430	237.72	-3.002	-3.096	N	Y
$v_7 = 4/v_5 = v_7 = 1$	26	0	1	25	0	1	53	1430	237.41	-2.991	-3.085	Y	Y
$v_6 = 2$	24	2		23	-2		49	1568	219.21	-3.098	-3.392	Y	Y
$v_6 = 2$	24	-2		23	2		49	1568	219.21	-3.098	-3.392	Y	Y
$v_6 = 2$	24	0		23	0		49	1589	219.02	-3.096	-3.420	N	N
$v_6 = 2$	26	2		25	-2		53	1590	237.47	-2.993	-3.319	N	Y
$v_6 = 2$	26	-2		25	2		53	1590	237.47	-2.993	-3.319	N	Y
$v_6 = 2$	26	0		25	0		53	1612	237.27	-2.991	-3.348	N	Y
$v_4 = v_7 = 1$	24	-1		23	1		49	1715	218.59	-3.093	-3.598	N	Y
$v_4 = v_7 = 1$	24	1		23	-1		49	1715	218.91	-3.091	-3.597	N	Y
$v_4 = v_7 = 1$	26	-1		25	1		53	1737	236.8	-2.988	-3.525	N	N
$v_4 = v_7 = 1$	26	1		25	-1		53	1737	237.15	-2.985	-3.524	N	Y
$v_4 = 1, v_7 = 2/v_5 = 2^0$	24	0	0	23	0	0	49	2032	219.49	-3.089	-4.055	N	Y
$v_4 = 1, v_7 = 2/v_5 = 2^0$	24	-2	0	23	2	0	49	2036	219.5	-3.092	-4.063	N	Y
$v_4 = 1, v_7 = 2/v_5 = 2^0$	24	2	0	23	-2	0	49	2036	219.53	-3.091	-4.063	N	Y
$v_4 = 1, v_7 = 2/v_5 = 2^0$	24	0	1	23	0	1	49	2036	218.49	-3.095	-4.064	N	Y

Table B1: (continued from previous page)

Vib. State	J_{up}	l_{up}	k_{up}	J_{lo}	l_{lo}	k_{lo}	g_{up}	E_{up} (K)	ν (GHz)	log A_{ul} (s^{-1})	log Int. (nm^2 MHz)	Det.	Cont.
$v_4 = 1, v_7 = 2/v_5 = 2^0$	26	0	0	25	0	0	53	2055	237.76	-2.984	-3.982	N	Y
$v_4 = 1, v_7 = 2/v_5 = 2^0$	26	-2	0	25	2	0	53	2058	237.78	-2.986	-3.990	N	Y
$v_4 = 1, v_7 = 2/v_5 = 2^0$	26	2	0	25	-2	0	53	2058	237.82	-2.986	-3.990	N	Y
$v_4 = 1, v_7 = 2/v_5 = 2^0$	26	0	1	25	0	1	53	2058	236.69	-2.990	-3.992	N	Y

This paper has been typeset from a TEX/LATEX file prepared by the author.